# Exploring Lithospheric Scale Structure in the Southern Yilgarn Craton with 3D Magnetotellurics

Alice Pascale van Tilburg

Department of Earth and Planetary Sciences

Faculty of Science and Engineering

Macquarie University

This thesis is submitted for the degree of Master of Research

November 2018

# Abstract

The electrical structure of the southern Yilgarn Craton is of interest in building an understanding of the pathways for mineralisation at the lithospheric scale. This project uses three dimensional inversion of magnetotelluric data from both broadband and long period stations to investigate an east west traverse of the South West, Youanmi and Kalgoorlie terranes of the Yilgarn Craton in Western Australia. These data are from the Southern Cross magnetotelluric survey. Previous studies in the region focussed on two dimensional modelling, however, phase tensor analysis of these data show a predominantly three dimensional subsurface that varies in strike across the profile. For this study models were produced using 26 stations, four of which contain data from an additional long period survey. The modelling highlights several conductive regions within a predominantly resistive subsurface. One large western conductor dominates the South West Terrane at depth, and a second more conductive feature is observed underneath the Kalgoorlie Terrane. These conductive regions may be associated with various mineralisation events during mantle activity prior to cratonization of the Yilgarn Craton.

# Acknowledgements

Sincere thanks to my thesis supervisor Dr Kate Selway, your support and guidance has been invaluable this year. You have encouraged me to challenge myself and give my best, which has not only benefitted this thesis, but will also carry over to my professional endeavours.

I would like to thank Professor M Dentith at University of Western Australia for providing me with the data for this thesis and to the Geological Society of Western Australia who partly funded its collection. I would also like to thank Shane Evans for providing information on the data collection and Moombarriga Geoscience and the Centre for Exploration Targeting at the University of Western Australia for providing me with processed .edi files and station data.

I am particularly grateful to the Australian Society of Exploration Geophysics for awarding me a tertiary student scholarship, and the opportunity to present my work at a society meeting.

Thank you to Sinan Ozaydin for your invaluable help with python scripts and problem solving.

Special thanks to my partner Alex for your care and knowledge. You have been instrumental in helping me with the coding required for this thesis and proof reading in the final weeks. I would also like to thank my family, Mum and Rhiannon, Adie, friends and Mres cohort for all your support this year.

# Contents

# Introduction

Conceptual models that describe Au and Ni mineralization in the Yilgarn Craton may be useful in characterising mineralisation in cratonic regions. The Yilgarn Craton is recognised globally for its world class gold and nickel deposits. These predominantly occur in the Kalgoorlie Terrane, but are also observed in the Youanmi Terrane (Barley & Groves, 1990). Mineral exploration strategies in the region have been primarily focused on crustal scale processes in order to locate further mineralised regions. However, investigating mantle scale processes within the craton is important to understand how these mineralised regions relate to lithospheric architecture (McCuaig et al., 2010). Geophysical studies provide us with the means to understand these processes. In the Yilgarn Craton seismic studies have characterised crustal structures such as faults and lithospheric structures such as the Moho and base of the craton (Fishwick & Reading, 2008; Reading et al., 2007). Aeromagnetic data have been used to aid classification of terranes at the surface and gravity data have been useful in delineating greenstone belts and identifying the margins of the Yilgarn Craton on the Australian continent (Blewett et al., 2010; Whitaker, 2001). Magnetotelluric (MT) surveys in the Yilgarn Craton have focussed on several different areas and include: the Youanmi survey in the north of the craton (Milligan, 2013), the EGF01 survey in the centre across the Kalgoorlie Terrane (Czarnota et al., 2008), the Albany-Fraser survey (Spratt et al., 2014) to the south east, and the Southern Cross survey in the south which crosses the South West Terrane, the Youanmi and the Kalgoorlie Terranes.

MT has been a useful tool for identifying some compositional changes including hydrogen in the mantle, graphites and sulphides (Jones et al., 2003; Livelybrooks et al., 1996; Selway, 2014). It delineates regions of electrically resistive earth from those that are more conductive. Mineralisation can be related to more geochemically enriched regions of lithosphere (Griffin et al., 2013). An example of using MT to image a mineral system is the Olympic Dam iron-oxide-copper-gold deposit in the Gawler Craton in southern Australia. MT data were able to image a large conductor ~30 km below known mineralisation, and were interpreted to relate to the processes forming the deposit (Heinson et al., 2018).

The Southern Cross Survey data provided by Mike Dentith and collected by Moombarriga Geoscience and the Centre for Exploration Targeting at the University of Western Australia are used in this thesis. Previous analysis of this data set was performed in 2D, with a focus on the crustal structure (Dentith et al., 2013). In this thesis, additional long period data not previously modelled are included with the Southern Cross data to perform a 3D inversion, focussing on

lithospheric structure. The aim of this thesis is to identify possible pathways for the mineralisation in the South West, southern Youanmi, and Kalgoorlie Terranes.

## Geological context

The Yilgarn Craton is found in south west Australia, and formed in the late Archean (Czarnota et al., 2010). It has a low gravity anomaly, and fast seismic velocity associated with low density lithosphere that is thick, depleted and typical of cratons (Blewett et al., 2010; Fishwick et al., 2005; Simons et al., 2002). Outcropping rocks of the upper crust in the Yilgarn Craton are comprised of Archean granites and greenstones characteristic of Archean terranes (Myers, 1995). These felsic regions are characterised by a slower seismic velocity (Rudnick & Fountain, 1995). Greenstone belts are of interest as they host the majority of Au and Ni mineralisation in the Yilgarn Craton and gravity data easily distinguishes the greenstone lithologies from less dense granitic rock. Greenstone units in this region include supracrustal rocks such as komatiite, basalt, andesite, volcaniclastic and meta-sedimentary packages (Blewett et al., 2010). Greenstone belts generally trend north-northwest across the craton  with a strike direction that is parallel to major faults (Anand & Paine, 2002; Goleby et al., 2006). The thickness of the lithosphere is estimated at 200 km from seismic tomography models ( Fishwick & Rawlinson, 2012; S. Fishwick & Reading, 2008)

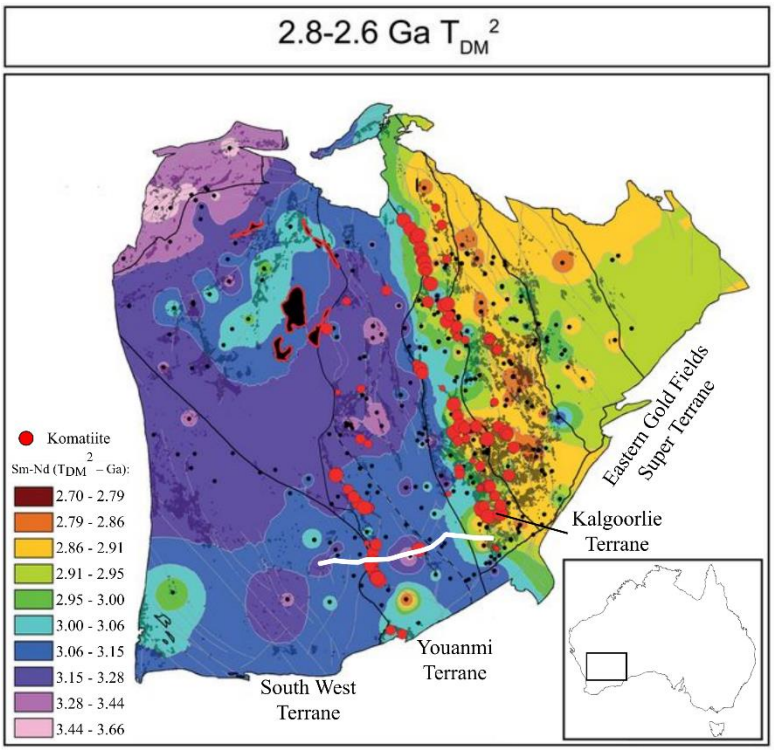


*Figure 1: Sm-Nd isotopic model ages for 2.8 to 2.6 Ga of the Yilgarn Craton. Komatiite emplacement occurs in the Youanmi Terrane and Eastern Goldfields Super Terrane, with the majority in the Kalgoorlie Terrane. The Southern Cross Survey line is shown by the white line. Adapted from (Mole et al., 2015)*

The Yilgarn Craton is subdivided into several terranes with the lithospheric structure determined predominantly by geophysical data sets. These include the Narryer Terrane in the north-west, the South West Terrane, the Youanmi Terrane in the centre and the Eastern Gold Fields Super Terrane (EGST) in the east (Cassidy et al. 2006 – GSWA record 2006/8) (Figure 1). Faults and shear zones are poorly magnetised compared with the moderate to highly magnetised felsic crust. This information, combined with geological mapping of faults, has been used to define terrane boundaries at fault locations (Myers, 1995; Whitaker, 2001, Cassidy et al. 2006). The EGST is further subdivided, with the Kalgoorlie terrane as the western subdivision, and is the most mineralised terrane in the region. The South West, Youanmi and Kalgoorlie terranes are the focus of this thesis. Previously the Youanmi Terrane was subdivided into the Murchison and Southern Cross domains, however significant differences in terrane properties are not observed in geochemical or seismic data sets. Champion and Cassidy (2007) used Sm-Nd model ages to outline a distinct difference in the western and eastern regions of the Yilgarn Craton and conclude a significant variation in relative age between the two blocks. In doing so, they found no distinction between the Murchison and Southern Cross domains and classified them as one terrane (Champion & Cassidy, 2007). Mole et al. (2015) compiled previous and current Sm-Nd isotopic data in Figure 1, which help to distinguish these two crustal blocks (Fig 1).

Komatiite hosted nickel sulphide deposits are abundant in the Youanmi and Kalgoorlie terranes. Nickel in the western terranes is mainly found in the southern Youanmi Terrane. This terrane has a Sm Nd model age of 2.9 Ga. The EGST has Sm Nd model ages of 2.7 Ga (Barnes, 2006). The formation of these deposits are thought to be two separate but similar events driven by mantle plumes which were directed eastward by the thicker crust in the west of the craton. This process may have reactivated the eastward margin, forcing komatiites to the surface (Mole et al., 2015). Gold in the region is structurally controlled and orogenic in nature, with mineral emplacement occurring across six deformation events post emplacement of Ni mineralisation (Blewett, et al., 2010). The largest Au deposits are found in Kalgoorlie and the western region of the EGST, with some mineralisation across the Youanmi and South West Terranes.

Craton wide models for komatiite mineralisation in the Yilgarn were initially suggested as a purely plume driven process, which caused mantle enrichment and significant partial melting of the crust and upper mantle. This model accounts for a hotter Archean mantle able to emplace komatiites into the crust (Campbell et al., 1989). Komatiites are mantle derived ultramafic rocks characterised by their high magnesium content (Arndt, 2003). Subduction has been argued as an alternative mechanism for accretion and emplacement of komatiites in the Yilgarn Craton using evidence from isotopic and geochemical data sets and by studying volcanism in the region (Barley et al., 2000;

Barley et al., 2008). Czarnota et al. (2010) suggests a geodynamic history of the EGST that combines these processes: an accretionary margin subjected to plume events, which undergoes periods of extension and compression by means of a subducting slab to the east of the craton.

A combined model is able to explain emplacement of komatiites requiring a high temperature, with the evidence in volcanics of a back arc tectonic environment. The accretionary process forming the Yilgarn involved a proto craton likely preserved in the Youanmi Terrane (Vielreicher et al., 2016) and a younger region of crust now the EGST. This is inferred from Sm Nd isotopic model ages (Champion & Cassidy, 2007). The younger crust that makes up the EGST may have only formed shortly before accretion (Reading et al., 2007). Czarnota et al. (2010) suggest that prior to subduction, at ~2.81 Ga, felsic rocks intruded into the crust in a rift tectonic setting. Following this event, a west dipping subduction zone developed at the edge of the EGST, followed by a period of compression in the region. During this subduction (~2.715 – 2.690 Ga) a large mantle upwelling emplaced komatiites into the EGST crust (Mole et al., 2015).Crustal delamination with slab rollback begins significant gold mineralisation (2.66 – 2.65 Ga). A further compression event at 2.665 – 2.640 emplaces the majority of the gold in the EGST.  Prior to cratonization, gold is further focussed into faults (Czarnota et al., 2010).

### South West Terrane

The South West Terrane is less endowed than any of the other terranes in the Yilgarn Craton (Hoatson et al., 2006). It is dominated by granites and granitic gneisses as opposed to the greenstone belts of the Youanmi and Kalgoorlie terranes, however it is unlikely that the South West Terrane was separate from the Youanmi Terrane post 3.1 Ga (Wyche et al., 2004). Seismic imaging of the terrane focussed on the deep crustal structure and imaged a fast seismic velocity zone at the base of the crust underneath Corrigin, 50 km west of the Southern Yilgarn Survey (Dentith et al., 2000). Explanations for this zone vary from mafic or ultramafic intrusions to mafic underplating relating to an extension event (Dentith et al., 2000). Underplating is where magmatic material ponds at the base of the crust (Thybo & Artemieva, 2013). The Moho in this terrane has been determined by seismic data as 38 km in depth, dipping gently to the east (Reading et al., 2003).

### Youanmi Terrane

The Youanmi Terrane is the central terrane imaged in the Southern Cross survey. It contains two major greenstone belts, the Forrestania and Lake Johnston greenstone units. Mineralisation in the region is confined to these units and is predominantly nickel sulphide hosted in komatiites (Wang et al., 1996). Nickel hosted komatiites in this region are 2.9 Ga in age. There is some gold in the region, however it is mostly found further north of the survey concentrated along faulting in the Forrestania Greenstone (Barnicoat et al., 1991).

Two previous MT surveys cross the Youanmi Terrane, EGF01 in the centre of the Youanmi and the Youanmi survey in the far north of the terrane. EGF01 had a focus on the Kalgoorlie region and found a resistive lithosphere in the Youanmi that dipped eastward underneath the Kalgoorlie Terrane (Czarnota et al., 2008). There was no conclusive evidence that the Ida Fault was imaged in the EGF01 survey. In the north, the Youanmi survey found a deep resistive zone across the east west traverse YU2, spanning the depth of the crust down to the Moho (Milligan, 2013). The Moho in the southern region of the Youanmi terrane has been determined at 38 km depth (Reading et al., 2007).

### Kalgoorlie Terrane

Kalgoorlie is the western most terrane of the EGST and is one of the richest regions in the world in gold mineralisation. Much of the gold is emplaced through the focussing of fluids in the upper and mid crust (Henson, 2006). This mineralisation often occurs in the footwall of faults (Blewett et al., 2010). Nickel is also a large resource and is hosted in komatiites with Sm-Nd model ages of 2.7 Ga (Champion & Cassidy, 2007). Important Nickel deposits in the southern Yilgarn include the Kambalda nickel camp in the Kalgoorlie terrane (Hoatson et al., 2006). In the craton centre, the Ida Fault has been mapped as a shallow fault, therefore if the fault is similar in the southern craton, only a small section of the Kalgoorlie terrane is mapped by the Southern Cross survey. MT in EGF01 maps a conductive lithosphere underneath the Kalgoorlie Terrane compared with the Youanmi Terrane (Czarnota et al., 2008). Seismic studies (Reading et al., 2007) image a Moho at 42 km depth.

# Theory

## Introduction

Magnetotellurics (MT) is a passive subsurface investigation technique involving the measurement of the Earth's magnetic and electric fields. This method is often used in conjunction with other geophysical tools such as seismic and gravity models when imaging and is particularly useful when resolving large scale lithospheric structures. The MT method was first described in Louis Cagniard's 1953 paper using time varying magnetic fields and electric 'telluric' currents to form resistivity profiles of the Earth (Cagniard, 1953). The source fields which produce these MT signals include solar wind for frequencies less than 1 Hz and thunderstorms or 'spheric' signals for the higher frequency fields (Cagniard, 1953). Maxwell's equations govern the application of these fields in describing conductive bodies, and their derivations allow us to compute one, two and three dimensional models of the subsurface. Magnetotelluric conventions are that z represents depth, while x and y represent the lateral directions. Dimensionality is defined by the complexity of the subsurface conductivity. A simple subsurface where conductivity only varies vertically (z direction) is a one dimensional Earth. A two dimensional Earth is defined by conductivity variation in both depth and a lateral (x or y) direction. A three dimensional Earth has variation along all three axes and may be comprised of several conducting bodies. I found 'Practical Magnetotellurics' (Simpson & Bahr, 2005) particularly useful for understanding MT theory.

## Maxwell's Equations

Maxwell's four equations describe the behaviour and generation of magnetic fields and the electric currents and fields associated with them.

Gauss' Law for electricity states that the electric field (E) through a closed surface is proportional to the charge (q) inside the surface, where $\varepsilon_0$ is the electric permittivity in free space.

$$\nabla \cdot \mathbf{E} = \frac{q}{\varepsilon_0} \tag{1.1}$$

Gauss's Law of magnetism states that the divergence of a magnetic field (B) is equal to zero, therefore magnetic monopoles do not exist.

$$\nabla \cdot \mathbf{B} = 0 \tag{1.2}$$

Faraday's Law of induction states that a time-changing magnetic field will induce an electric current proportional to the incident magnetic field.

$$\nabla \times \mathbf{E} = -\frac{\partial \mathbf{B}}{\partial t} \tag{1.3}$$

Ampere-Maxwell's Law states that the magnetic field produced from a closed loop is proportional to the electric current moving through the loop, where $\mu_0$ is the permeability of free space and **j** is the total electric current density.

$$\nabla \times \mathbf{B} = \mu_0 \varepsilon_0 \frac{\partial \mathbf{E}}{\partial t} + \mu_0 \mathbf{j} \tag{1.4}$$

The following material properties describe electric and magnetic fields in rocks:

- Conductivity (σ) $Sm^{-1}$: the ability of a material to carry an electric current. Resistivity ρ is the inverse of conductivity. Ohm's law relates current density to conductivity.

$$\boldsymbol{j} = \sigma \boldsymbol{E} \tag{1.5}$$

- Electric permittivity (ε) $Fm^{-1}$: the ability of a material to form an electric field inside it, where D is the electric flux density.

$$\boldsymbol{D} = \varepsilon \boldsymbol{E} \tag{1.6}$$

- Magnetic permeability (μ)$Hm^{-1}$: the ability of a material to form a magnetic field inside it, where B is the magnetic field of the material and H is the magnetising field strength.

$$\boldsymbol{B} = \mu \boldsymbol{H} \tag{1.7}$$

## Assumptions of the Magnetotelluric Method

The following assumptions are integral to the magnetotelluric method (Cagniard, 1953):

1. Maxwell's equations (1.1 – 1.4) are obeyed
2. The Earth only dissipates or absorbs electromagnetic (EM) energy
3. All EM fields are treated as conservative and analytic away from their sources
4. MT source fields are generated sufficiently far away such that they can be assumed to act as a plane wave.
5. In a one dimensional layered Earth, charges do not accumulate, however in a multidimensional Earth, charges may accumulate along boundaries/discontinuities – as such the Earth behaves as an ohmic conductor and Equation 1.5 is satisfied.
6. The effects of bulk rock conductivity are far larger than the effects of the permittivity and permeability of the rock, thus the free space values
   $\varepsilon = 8.85\ e^{-12}\ Fm^{-1}$ and $\mu = 1.2556\ e^{-6}\ Hm^{-1}$ are applied.
7. Time varying displacement currents are negligible in comparison to the time varying conduction currents. Thus, EM induction in the Earth is treated as a diffusive process and displacement currents can be neglected in Equation 1.4.

## Frequency Domain and Skin Depth

MT data are collected as a time series of orthogonal electric and magnetic fields. The variation of these fields in time is assumed to be a harmonic oscillation, represented by the angular frequency omega (ω). These fields are described through diffusion equations, and are converted from the time domain to the frequency domain via Fourier transform.

Using the above assumptions, for a homogenous half space, Maxwell's equations can be solved in the frequency domain to produce Equations 2.1 and 2.2. These equations describe the electric field and magnetic intensity as a function of depth (z), time (t) and angular frequency (ω).

$$E_x(z,t) = E^t e^{-k_1 z} e^{-i\omega t} \tag{2.1}$$

$$H_y(z,t) = \frac{1}{i\omega\mu} E^t(-k_1) e^{-k_1 z} e^{-i\omega t} \tag{2.2}$$

The last term in both equations describes a complex sinusoidally varying field. The decay of this field is also described by the complex number ($k_1$), which is the propagation constant and is defined by:

$$k_1 = (1+i)\sqrt{\frac{\omega\mu\sigma}{2}} \tag{2.3}$$

The inverse of Equation 2.3 describes the penetration depth of an electromagnetic wave into a conductor. This is known as the skin depth δ. From the right hand side of the equation we show that shorter frequencies (f) (longer periods) have a much larger skin depth, thus imaging the Earth to a greater depth.

$$\delta(\omega) = \sqrt{\frac{2}{\mu_0 \sigma \omega}} \approx \frac{503}{\sqrt{f\sigma}} \tag{2.4}$$

## Impedance and the Impedance Tensor

A propagating electromagnetic wave has orthogonal electric and magnetic field components. The ratio of the electric field and magnetic field intensity components is known as the impedance (**Z**). Equation 3.1 relates an x direction electric field (**E**x) to the orthogonal y direction (**H**y) magnetic field intensity component for a plane wave. The impedance is a complex number.

$$\boldsymbol{Z}(\omega)_{xy} = \frac{\boldsymbol{E}(\omega)x}{\boldsymbol{H}(\omega)y} = \frac{-i\omega\mu}{k1} \tag{3.1}$$

Impedance is also represented as a tensor, shown as a frequency dependant matrix in Equation 3.2 (Weaver et al., 2000).

$$\mathbf{E} = \mathbf{ZH} \text{ or } \begin{pmatrix} E_x \\ E_y \end{pmatrix} = \begin{pmatrix} Z_{xx} & Z_{xy} \\ Z_{yx} & Z_{yy} \end{pmatrix} \begin{pmatrix} H_x \\ H_y \end{pmatrix} \tag{3.2}$$

For a uniform half-space of the Earth, combining Equations 2.3 and 3.1, it can be shown that the impedance relates as:

$$|Z_{xy}(\omega)|^2 = |\frac{E_x(\omega)}{H_y(\omega)}|^2 = \frac{\omega\mu_0}{\sigma} \tag{3.3}$$

$$\rho = \frac{1}{\omega\mu_0}|Z_{xy}|^2 = \frac{1}{\omega\mu_0}|\frac{E_x}{H_y}|^2 \tag{3.4}$$

Equation 3.4 is the resistivity found from the xy component of the Z tensor. It returns a resistivity that represents an average across a radius of subsurface determined by skin depth. Where the Earth is not uniform, this calculated resistivity is known as the apparent resistivity $\rho_a$. Using the average resistivity for a chosen frequency infers that MT is a good technique for delineating conductive bodies, but may have difficulty delineating boundaries of resistive layers. In particular, a large conductor will bring up the average resistivity across a chosen frequency, effectively masking the boundaries of resistive regions beneath it.

The impedance tensor **Z** contains both real and imaginary parts which resolve into a magnitude and phase ($\phi$) component. The phase is found by taking the arctan of the impedance and is the phase shift between the electric and magnetic components and can also be written as a ratio of the imaginary and real components of the impedance tensor.

$$\phi(\omega) = \tan^{-1}\left[\frac{E_x(\omega)}{H_y(\omega)}\right] \tag{3.5}$$

$$\phi(\omega) = \tan^{-1}\left[\frac{Im\, Z_{xy}(\omega)}{Re\, Z_{xy}(\omega)}\right] \tag{3.6}$$

## Dimensionality

For a given impedance tensor(Booker, 2014; Caldwell et al., 2004):

$$\mathbf{Z} = \begin{pmatrix} Z_{xx} & Z_{xy} \\ Z_{yx} & Z_{yy} \end{pmatrix} \tag{4.1}$$

In a one dimensional Earth Zxy and Zyx should be equal with opposing signs even as the tensor is rotated. For a one dimsional Earth all vertical field vectors are zero. A single station could be used

to map the simple layering at one spot on the Earth, and the only changes in the subsurface occur across the depth (z) axis.

$$\mathbf{Z} = \begin{pmatrix} \mathbf{0} & \boldsymbol{a} \\ -\boldsymbol{a} & \mathbf{0} \end{pmatrix} \tag{4.2}$$

A two dimensional Earth has a change in resistivity along the y axis. When x and y are aligned parallel and perpendicular to geoelectric strike, the tensor reduces to Eq. 4.3. Additional seismic or geological information is used to delineate which component (yx or xy) corresponds to the geoelectric strike direction, which is  the direction in which the subsurface conductivity does not vary.

$$\mathbf{Z} = \begin{pmatrix} \mathbf{0} & \boldsymbol{Z_{xy}} \\ -\boldsymbol{Z_{yx}} & \mathbf{0} \end{pmatrix} \tag{4.3}$$

Three dimensionality varies across all axes. In this case the impedance tensor will have non-zero Zxx, Zyx, Zxy and Zyy components:

$$\mathbf{Z} = \begin{pmatrix} \boldsymbol{Z_{xx}} & \boldsymbol{Z_{xy}} \\ \boldsymbol{Z_{yx}} & \boldsymbol{Z_{yy}} \end{pmatrix} \tag{4.4}$$

## Phase Tensor Analysis

Phase information contained in magnetotelluric impedance data can be represented as a second rank tensor known as the phase tensor (Caldwell et al., 2004). The phase tensor is useful for determining the dimensionality of the subsurface through diagnostic techniques including ellipticity, skew, and strike. Phase tensors provide information on the regional subsurface while remaining undistorted by features unresolvable at small scale.

The MT phase tensor ($\mathbf{\Phi}$) includes X and Y, the real and imaginary parts respectively, of the impedance tensor Z.

$$\mathbf{\Phi} = \boldsymbol{X}^{-1}\mathbf{Y} = \begin{pmatrix} \mathbf{\Phi}_{xx} & \mathbf{\Phi}_{xy} \\ \mathbf{\Phi}_{yx} & \mathbf{\Phi}_{yy} \end{pmatrix} \tag{5.1}$$

This relationship can also be shown graphically with an ellipse (Figure 2).

This image has ben supressed. Please see Caldwell 2004

*Figure 2: Graphical representation of the phase tensor from Caldwell, 2004 where the angle alpha minus beta is the direction of the major axis of the ellipse. A circle indicates a 1D subsurface while an ellipse indicates a complex subsurface. Beta is the skew angle. Skew values more than 3 indicate a three dimensional subsurface.*

### Ellipticity

The ellipticity is defined by the shape, or distortion of the phase tensor. Spherical tensors have an ellipticity of one and indicate a one dimensional Earth, while a distorted tensor is representative of a more complex subsurface. The ellipticity describes how strongly the currents within the earth follow a particular direction. The ellipticity (**λ**) is defined by (Bibby et al., 2005)

$$\boldsymbol{\lambda} = \frac{|\boldsymbol{\Phi_a} - \boldsymbol{\Phi_b}|}{\boldsymbol{\Phi_a} + \boldsymbol{\Phi_b}} \tag{5.2}$$

### Skew

Skew (**β**) is a measure of deviation of electric field flow from the parallel magnetic field. Skew values at 0 are considered two dimensional, however errors in data allow for a quasi 2D structure to be interpreted at values out to 3 degrees. Skew values >3 are generally accepted as 3D structure (Booker, 2014).

$$\boldsymbol{\beta} = \frac{\mathbf{1}}{\mathbf{2}}\mathbf{tan}^{-\mathbf{1}}\left(\frac{\boldsymbol{\Phi_{xy}} - \boldsymbol{\Phi_{yx}}}{\boldsymbol{\Phi_{xx}} + \boldsymbol{\Phi_{yy}}}\right) \tag{5.3}$$

### Strike

The geo-electric strike shows the orientation of current flow in the subsurface. It is a useful tool for assessing possible structural change, complexity and the most useful inversion tool to use (1D, 2D or 3D). In two dimensional modelling this is used to check for off profile 3D features affecting the model. For a 2D model, the strike must be consistent with period from station to station. If the strike varies along the profile or across the array then a 3D is suitable for assessing complex subsurface features.

## Causes of conductivity in a resistive lithosphere

Magnetotellurics is sensitive to conductive regions in the subsurface which occur due to the flow of electrical charge. This can be from conductive minerals such as graphite films at grain boundaries, interconnected sulphide mineralisation and hydrogen enrichment in the lithosphere (Selway, 2014). Thermal changes also affect conductivity, where higher temperatures have a higher conductivity, such as at the base of the lithosphere heated by the mantle (Leary & Phinney, 1974). Thus, conductive regions can include melts, regions of enriched lithosphere, and thermal anomalies from the mantle. This assists in constraining regions of possible mineralisation, such as Olympic Dam (Heinson et al., 2018).

# Data

## Station Data

The data used for this project were provided by Prof. M Dentith (University of Western Australia) and were recorded by Moombarriga Geoscience and the Centre for Exploration Targeting at the University of Western Australia across three campaigns. Stations STY01 – STY38 were collected in October 2009 and extension stations STYE01 – STYE08 were collected in December 2012. STYE are the broadband stations and have a period range of 0.00312 s to 595 s, and each station recorded approximately two days of data. STYE stations recorded at longer periods up to 2941 s and were recording up to 41 days. Long period (LP) stations LP02 – LP39 were collected in January 2014 and are co-located with the broadband STY stations. Their maximum period reaches 3744 s and stations were recording for up to 22 days. Detailed location and recording durations of the STY and STYE stations can be found in Dentith et al., 2013. Broadband data stations STY and STYE were already processed by Moombarriga Geoscience and in .edi file format. Long period stations were received in time series format and had not been previously processed or included in inversions. This was due to instrumentation and noise problems during data collection. Their quality had never been fully investigated (M. Dentith, pers. comm.).

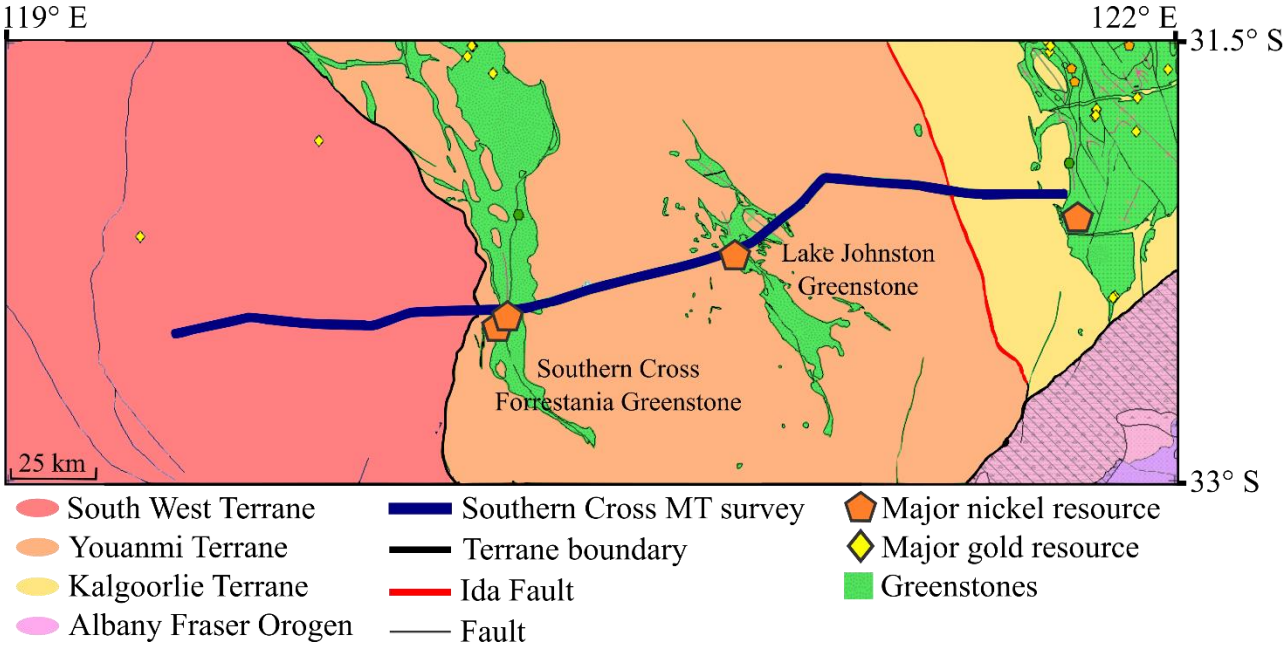


*Figure 3: Location of the Southern Cross survey. Located in the southern region of the Yilgarn Craton, the 300 km survey spans three terranes and several major komatiite associated nickel deposits located in greenstone belts. Adapted from maps from the Western Australian Department of Mines, Industry Regulation and Safety GeoVIEW: https://geoview.dmp.wa.gov.au/GeoViews.*

The stations are located across a 300 km east west traverse across the Southern Cross Domain, extending into sections of the South West and Kalgoorlie terranes. The traverse crosses several

interesting geological features including the Southern Cross and Forrestania greenstone belts, the Southern Kawana fault system, the Koolyanobbing Shear Zone, and the Ida Fault. Close by to the survey are the Flying Fox and Good Morning nickel mines in the Forrestania Greenstones, and the Emily Ann nickel mines in the Lake Johnstone Greenstones which have global nickel grades of 1.91% and 3.62% respectively (Hoatson et al., 2006).

## Processing of Long Period Data

Broadband stations were already processed by Moombarriga Geoscience while long period data were received in time series format with no prior processing. The raw data for each station were plotted to determine if the set contained four or more days of continuous high signal to noise data. Figure 4 shows station 30 LP data, which exhibits regions of noise and anomalies which are prevalent across much of the LP data set in the Ex and Ey channels. Additionally, the magnetic signal was noisy throughout the data set. The magnetic field noise presented as an odd shape across the entire recording, rather than short noisy sections. Continuous data for each station was compiled into a single time series file.

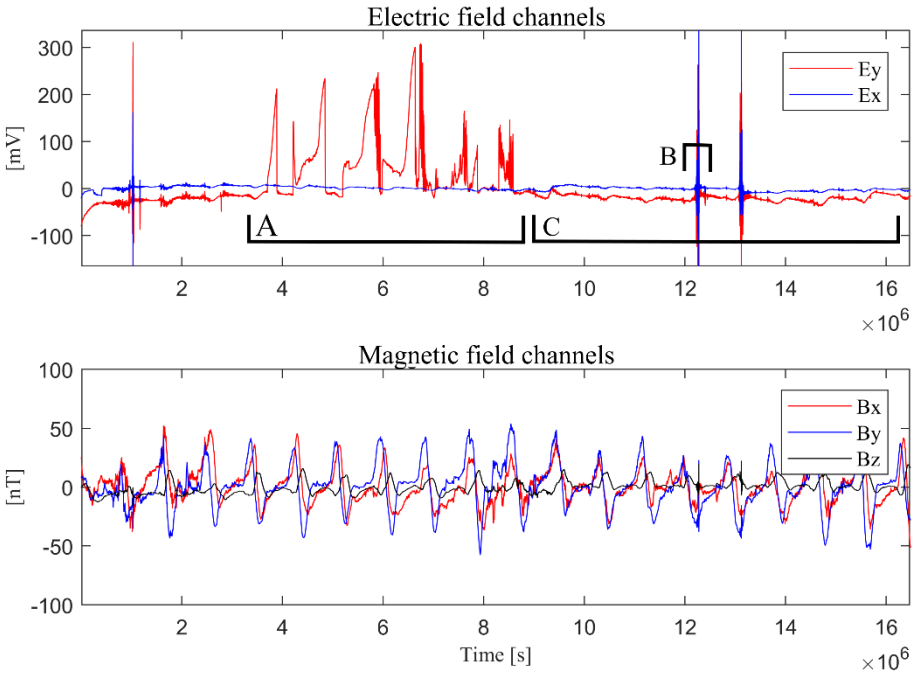


*Figure 4: Long period station 30 time series data. A) Noisy Ey data indicating a problem with Ey sensor during data collection. B) Spikes of noise in the electric fields which are filtered out during Fourier transform. C) Example of continuous MT time series data. For station LP30 approximately 10 days of clean data were used. The magnetic field channels also show some noise not typical of MT data. This noise exists across most of the LP stations.*

Egbert's code (Egbert, 1997) was used to process the time series data. First the data are Fourier transformed to the frequency domain. Then impedances are calculated. This code is also used to remote reference the data sets. Remote referencing uses matching magnetic fields to obtain estimates of the impedance tensor thus removing noise from the data set (Gamble et al., 1979). Remote referencing is particularly useful in the dead band where low intensity signals are obscured by the high signal to noise ratio. The dead band represents a range of periods between 1 and 10 s, where intensity of the incident magnetic field is often low. An example of dead band data from Station 17 is shown in Figure 6 where remote referencing has not been performed. Remote referencing was performed by Moombarriga Geoscience on STY and STYE data. Due to mis-alignment of the magnetic fields and difficulties with data quality, remote referencing did not improve the data quality for the long period stations (LP).

Processing of the long period stations yielded four stations with high enough quality to be used for inversion. At this stage of processing, many stations were excluded because they did not have enough continuous data to extract information at periods longer than the STY and STYE stations. Stations were further excluded based on erratic apparent resistivity plots, or when the phase did not match that of the co-located broadband station.

### Apparent Resistivity and Phase

Equations 3.4 and 3.6 were used to plot the apparent resistivity and phase for the Zxy and Zyx components for each station with errors.  Figure 5 gives an example of this in the STY19 broadband sation data set, and Figure 6 is an example of data from LP stations. All apparent resistivity and phase data can be found in the supplementary material.

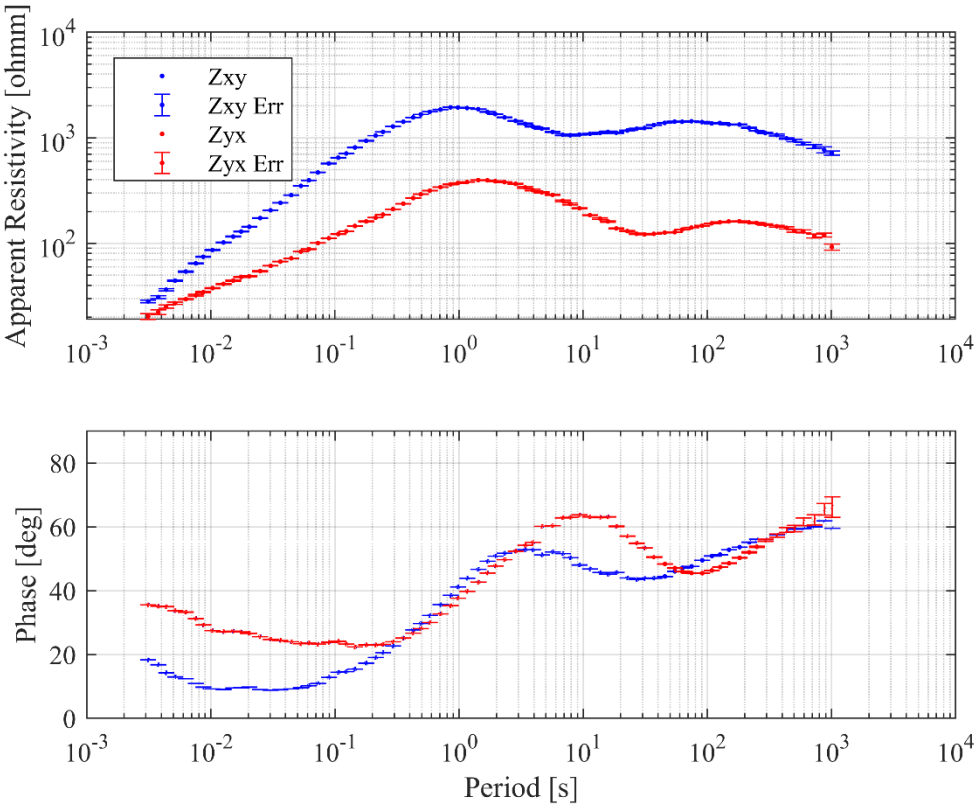


*Figure 5: Example of apparent resistivity and phase data from broadband station 19.*

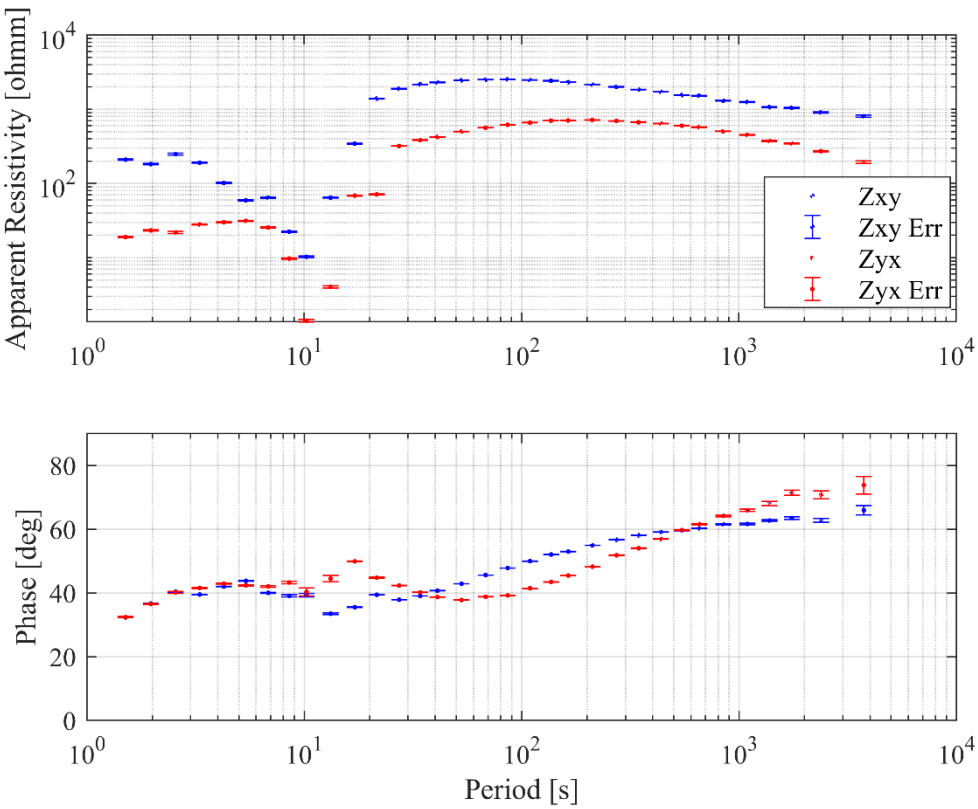


*Figure 6: Example of dead band data and long period apparent resistivity and phase from LP Station 17*

## Stitching Broad Band and Long Period Data

Broad band and long-period stations were co-located, so the processed data files were stitched into single files to be used for further analysis. This overcame the problems associated with the poor quality dead-band periods in the long-period stations since broadband data for these periods were of good quality. Figure 7 and Figure 8 display data pre and post stitching for broadband and long period station 6. Apparent resistivity curves for co-located stations were different in magnitude. This is likely due to static shift from galvanic effects in shallow regions (Ogawa & Uchida, 1996) . To account for this the electric field components were altered by changing the scaling factor during processing. This shifted the apparent resistivity curves to match the broadband stations.

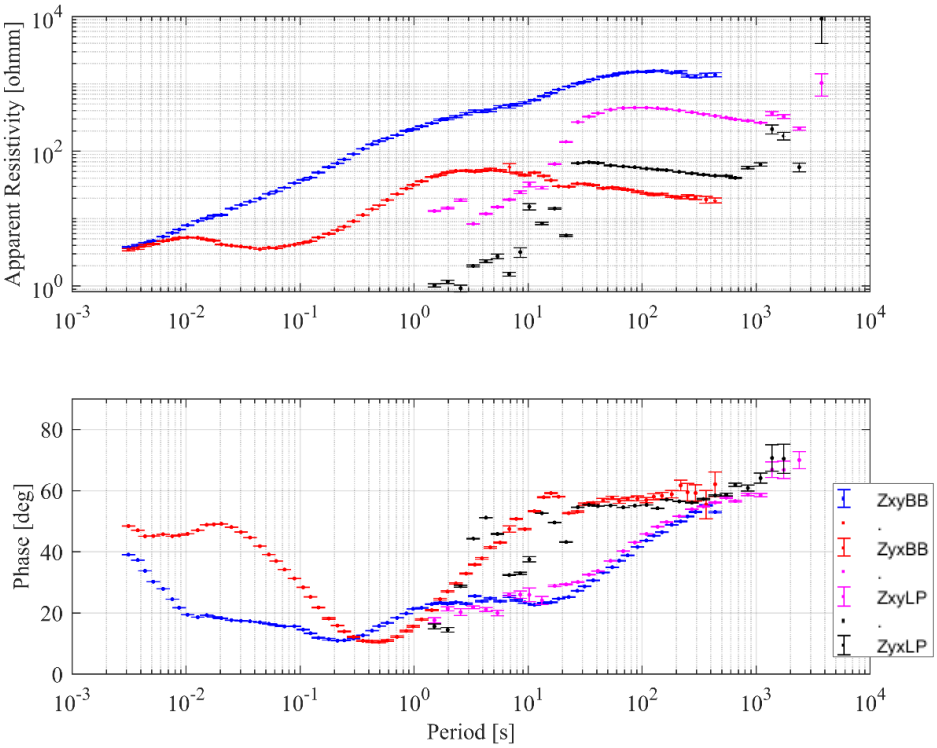


*Figure 7: Station 6 pre stitching.*

*This plots the broadband data and long period data for apparent resistivity and phase curve comparison.*

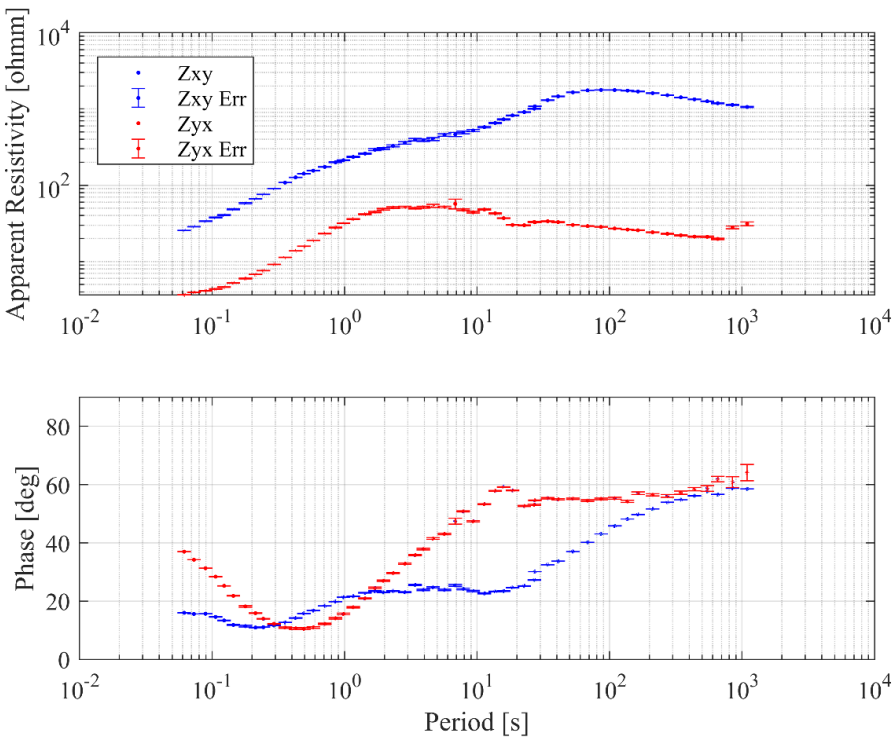


*Figure 8: Apparent resistivity and phase of station LP6 post stitching.*

.

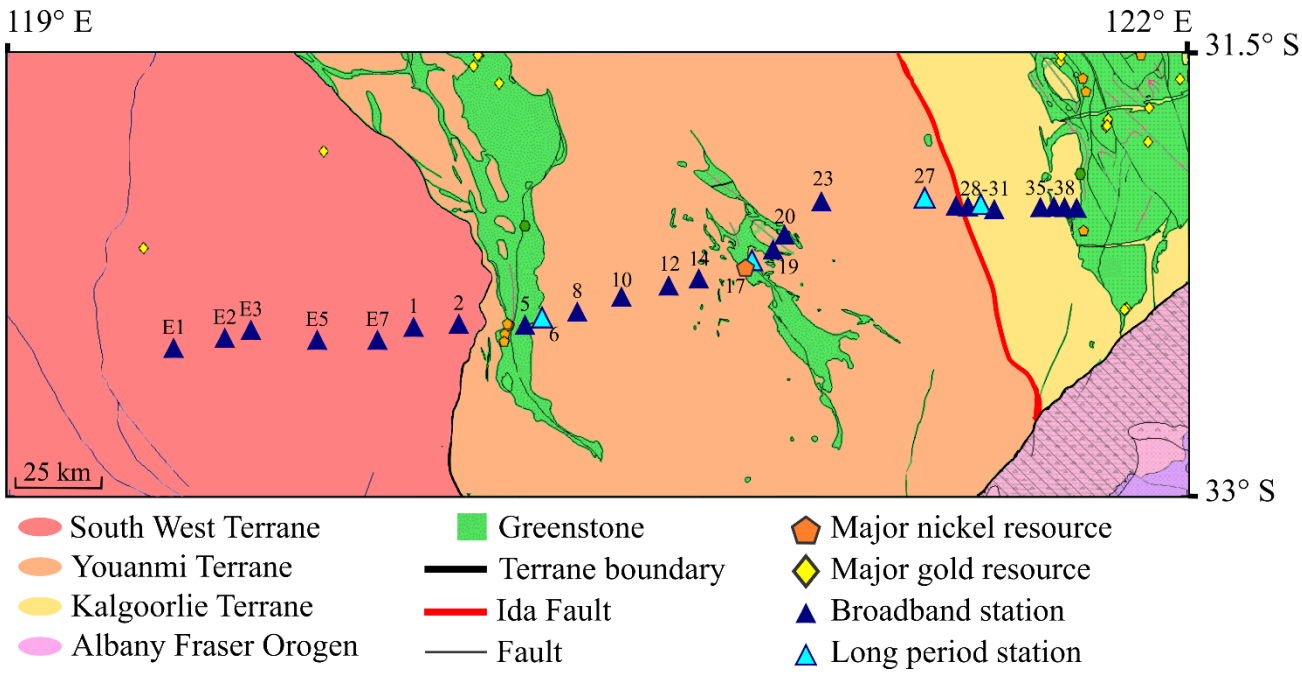


*Figure 9: Final stations included for inversion. There are 26 stations in total with 4 long period stations.*

The final location of the 22 broadband stations and four long period stations selected for inversion are detailed in Figure 9. All stations had a lower period limit of 0.15 s for inversion. Seven stations included across the South West Terrane used periods up to 2380 s. Broadband stations across the Youanmi Terrane included periods from 0.15 s to 595 s. Long period stations had periods out to 3744 s, but due to data quality only periods out to 2380 s were included for inversion. Four long period stations were included from the given data sets. The Kalgoorlie Terrane included five broadband stations, most of which included data out to 2380 s.

## Phase Tensor Analysis

Phase tensors were used to determine the dimensionality of the Southern Cross data. If a 3D subsurface is inverted with a 2D scheme, anomalous features may be present in the model which may not accurately represent the subsurface structure (Ledo, 2005). Phase tensor analysis was performed on both the broadband and long period data sets. The aim of this analysis was to measure the dimensionality of the subsurface and identify regions of complexity which may be of interest during modelling. Figure 10 and **Error! Reference source not found.** are examples of the visualisation used for phase tensor analysis in this thesis. Ellipticity, skew, and strike were plotted for each station, and the ellipticity and strike were plotted spatially for all stations at four different periods.

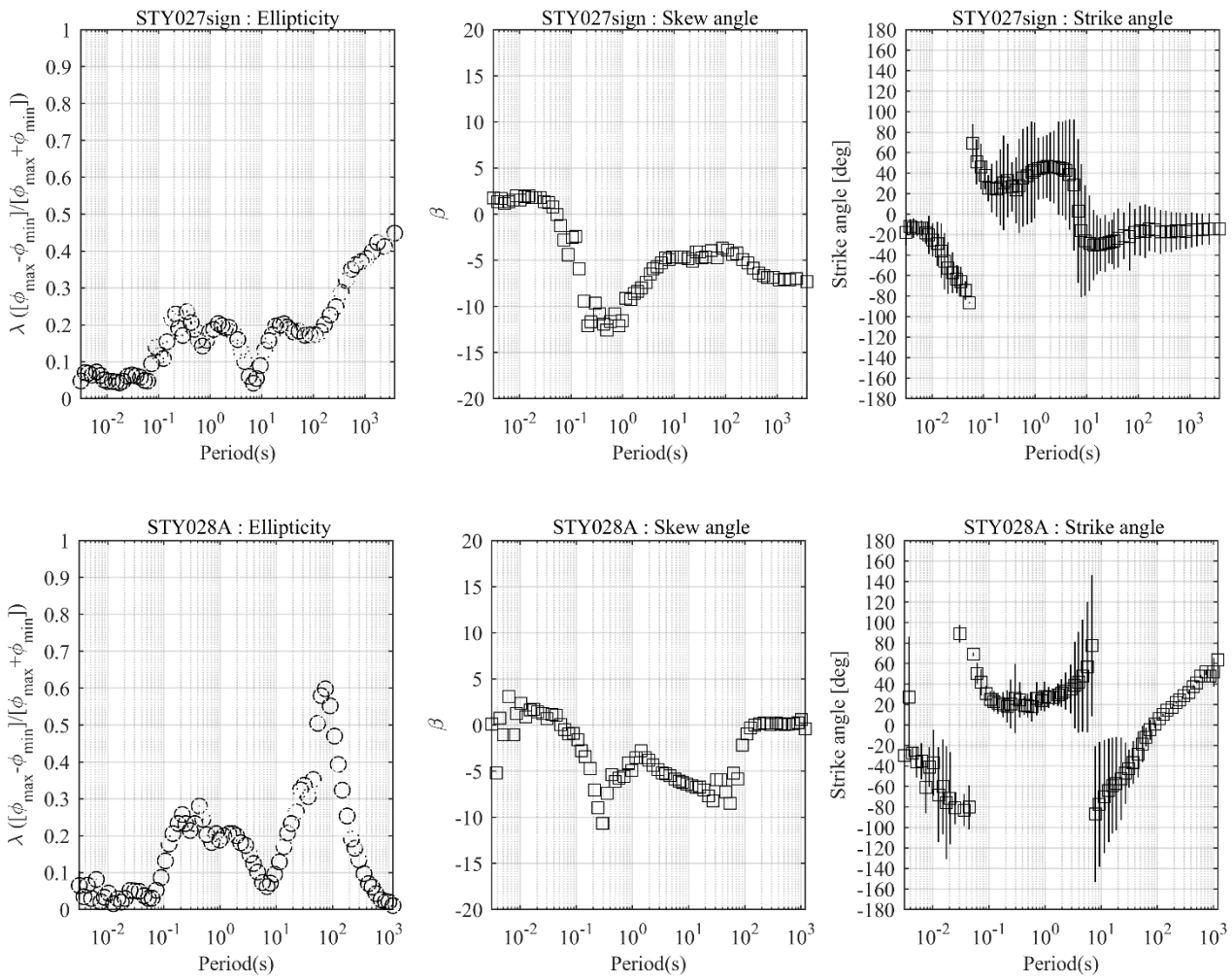


*Figure 10 Example for stations LP27 and STY28 of ellipticity skew and strike, which indicate a complex subsurface that is 3D in nature, with some quasi 2D regions at short periods. Plots created using code by* (Thiel, 2008)

## Ellipticity

In general, values above 0.1 for ellipticity indicate a more complex subsurface which is not 1D (Caldwell et al., 2004). At Station 28 the shallow subsurface is close to circular, while periods beyond 1 s show ellipticity values up to 0.6. This indicates an increase in complexity with period (depth). For these periods there is strong directional flow of current. Station 27 has much lower ellipticity values at these periods, only becoming more complex and with strongly oriented currents at depth. Ellipticity across the entire survey was usually more than 0.1, except for at very short periods which were not included in the inversion, and at long periods in stations further east than STY28.

### Skew

Skew values above 3 indicate a complex 3D earth. Station 28 shows absolute skew values as high as 10 for periods between 0.1 and 10 s, indicating 3D structure. Station 27 has similar skew values at 0.1 s, however has a high skew value at long periods. Skew values are highest between periods 0.1 – 50 s in eastern stations STY23 – STY31 suggesting there is some complex structure causing deviation of the electric field. A similar but less robust complexity (skew values just over 5) is observed in stations below the western area of the Youanmi Terrane at depth.

### Strike

Strike across the survey has several consistent regions. At 90 s period and less, there is a consistent EW strike appearing in the extension stations of the South West Terrane. This is detailed in **Error! Reference source not found.**. Stations STYE4 and STYE5 have strike perpendicular to the other stations. There is a 90 degree ambiguity in strike direction from phase tensors (Caldwell et al., 2004), so perpendicular station results may be indicating the same feature. We expect the majority of features in the region to have a north south strike as these are the strike of geological features in the region. **Error! Reference source not found.** highlights some of these features (faults) that e xpress at the surface. At 90 s the majority of ellipses across the Youanmi Terrane are aligned east west, however at 505 s the strike is constantly changing. The geoelectric strike direction in the Kalgoorlie Terrane has strong variation across all periods.

### Dimensionality

The Southern Cross survey indicates overall a three dimensional subsurface due to high skew across every station and a strong ellipticity and varying strike direction. Several regions of interest can be drawn from this analysis. First, a feature with high ellipticity in the South West Terrane which changes from an orientation of approximately 20 degrees at short periods to a consistent strike of 80 degrees at long periods. Across the entire survey the most complex and 3D regions occur between periods of 1 and 10 s, and a drop in complexity is noted at the longest periods. In the east, a strong complex 3D feature is apparent, with a more 2D region directly beneath it. The phase tensor plots in **Error! Reference source not found.** highlight complexity between the Kalgoorlie Terrane and the western terranes. This difference is defined by a stronger ellipticity but often more consistent strike in the west, with a much more inconsistent strike under Kalgoorlie.

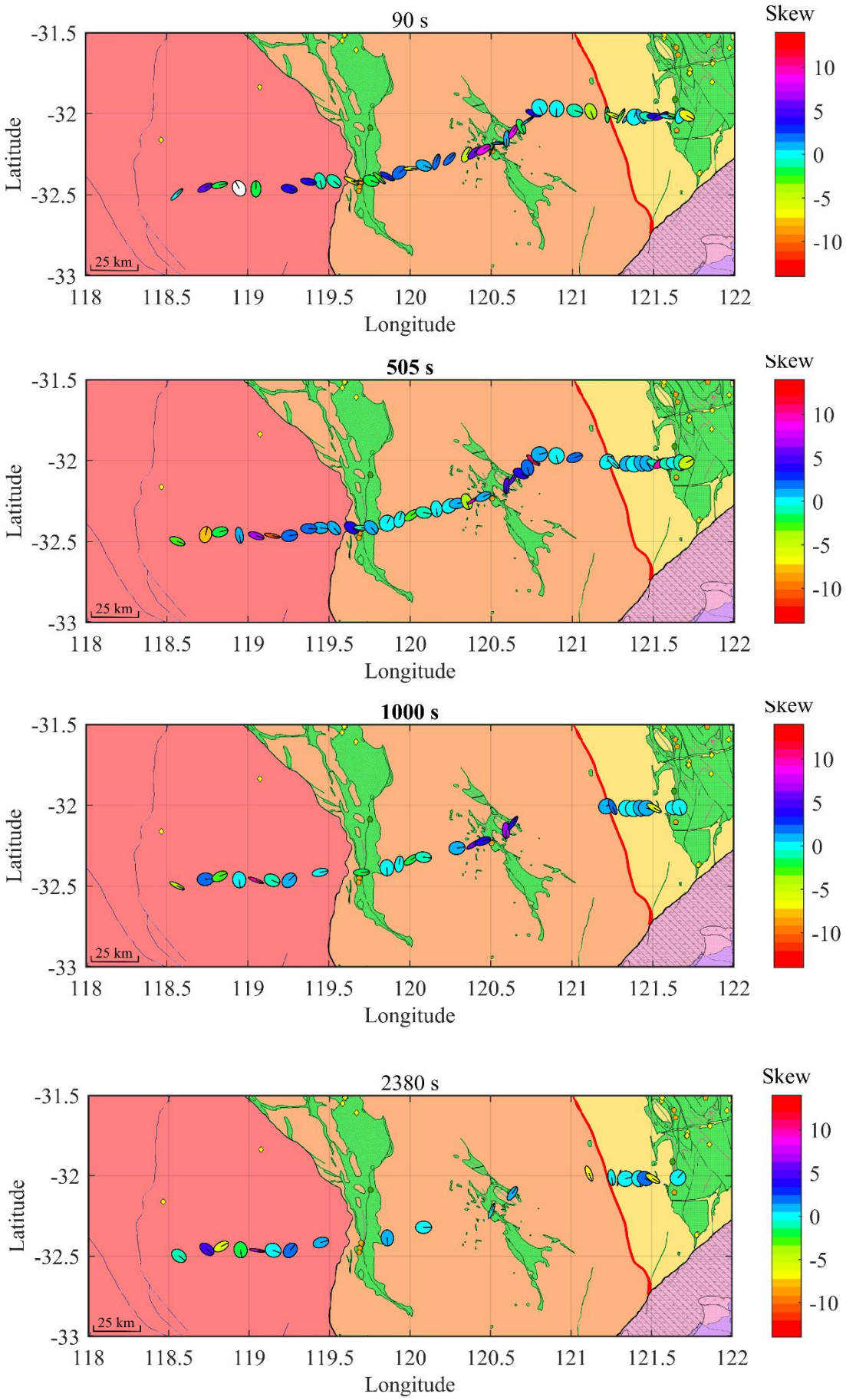


*Figure 11: Phase tensor analysis for a range of periods.*

# Modelling

## Method

Modelling was completed in 3D using ModEM3DMT (Egbert & Kelbert, 2012; Kelbert et al., 2014). The inversion scheme used by ModEM computes the minimization of a penalty functional described in Equation 6.1. This method uses the data d to fit the earth conductivity model parameter m. Parameters included in the inversion process are f(m), for forward mapping, $C_d$, the covariance of data errors, ν, the trade-off parameter, $m_0$, the prior model parameter, and $C_m$, the model covariance (Kelbert et al., 2014).

$$\Phi(\mathrm{m},\mathrm{d}) = \left(\mathrm{d} - \mathrm{f}(\mathrm{m})\right)^{\tau} C_m^{-1}(\mathrm{d} - \mathrm{f}(\mathrm{m})) + \mathrm{v}(\mathrm{m} - m_0)^{\tau} C_m^{-1}(\mathrm{m} - m_0) \tag{6.1}$$

ModEM uses a data space approach over a model space approach. This reduces the size of the matrix when computing the problem which cuts computation time considerably (Siripunvaraporn et al., 2005). The inversion is computed by minimizing the functional using non-linear conjugate gradients. This method computes the forward problem at each iteration, resulting in faster convergence of the model (Rodi & Mackie, 2001). The model converges when it is unable to leave a local minimum.

Variables in this model which I have changed in the modelling process include the resistivity of the starting model and the applied covariance. Three approaches I used during modelling included finding the model with the best fit, constraining features in the model, and finding a model which best represents the geological features of the region. Table 1 outlines the starting conditions of each model and their final root mean square (RMS) misfits. The best model fit was defined by the model with the lowest RMS and the individual fits for each station. Model fitting is performed by comparing the station data to the inverse model responses for the final iteration of the inversion as seen in Figures 13 - 19. I used low resistivity starting models to constrain highly resistive features and high starting resistivity models to constrain conductive features in the region. I ran models with different covariance values to understand where features appeared at depth relative to the known geological features. Model covariance is a matrix which defines the model norm. Is describes the smoothness and magnitude of resistive variation to the base model (Siripunvaraporn et al., 2005). Low covariance was used to investigate model fits of features to stations and a high covariance was used to smooth out station features at depth.

I used data from 26 stations in the inversion. Initial modelling included data from the entire period range (0.00312 – 2380 s). In order for static shift effects to be more easily modelled and due to a

strong interest in lithospheric structure over upper crustal structure, periods shorter than 0.15 s were not included in the final inversions. The final range of periods included for inversion was from 0.15 s to 2380 s. By not including these short periods, resolution in the uppermost few kilometres is poor. Zxx and Zyy are are the off diagonals of the impedance tensor, which are non-zero in 3D regional data. These elements were given a 10% error floor to fit during inversion, while Zxy and Zyx were given only a 5% error floor.

*Table 1: Model parameters for inversion and their final RMS misfit*

| Model | Covariance | Starting Resistivity (Ω m | RMS |
|---|---|---|---|
| A | 0.3 | 100 | 1.928354 |
| B | 0.3 | 10 | 1.963777 |
| C | 0.3 | 1000 | 2.047308 |
| D | 0.2 | 100 | 2.013814 |
| E | 0.6 | 100 | 2.111788 |
| F | 0.6 | 500 | 2.104472 |
| G | 0.6 | 1000 | 2.435089 |
| Un-rotated F | 0.6 | 500 | 2.405829 |

Modelling was conducted with a dense mesh surrounded by larger padding cells. Figure 12 graphs the mesh over station locations. The model mesh was rotated 20 degrees west of north to align the mesh along the profile of the stations. In the descriptions of the modelling that follow, north and south move along the X axis of the grid and east and west move along the Y axis of the grid. The dense mesh was gridded at 2.5 x 2.5 km and extended 25 km north and south of the stations. The dense mesh extended 35 km east and west of furthest stations. The padding cells extended 20 blocks outside the dense mesh with an increment factor of 1.2 starting at 5 km. The model was 55 layers deep with an increment factor of 1.2. The final mesh size was ~1000 x 1000 km with a depth of 1200 km. Models were generated using the Macquarie University Earth and Planetary Sciences cluster Toto and on the national computation infrastructure NCI Australia.

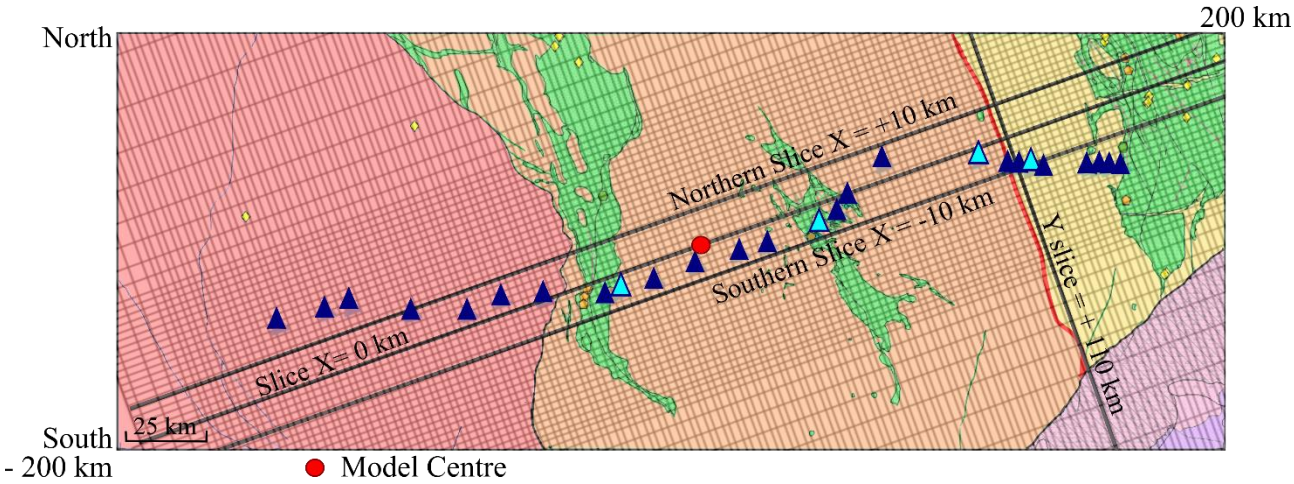


*Figure 12: Map of the dense mesh at 2.5 by 2.5 km squares overlaid on the survey area, with 25 km north and south of stations and 35 east and west of stations. Slices X = 0 X = +10 and X = - 10 are the cross sections used in model figures. Y slice 100 km is a perpendicular view at 110 km along the survey.*

## Models

### Model A

Starting Resistivity 100 Ω m and covariance of 0.3

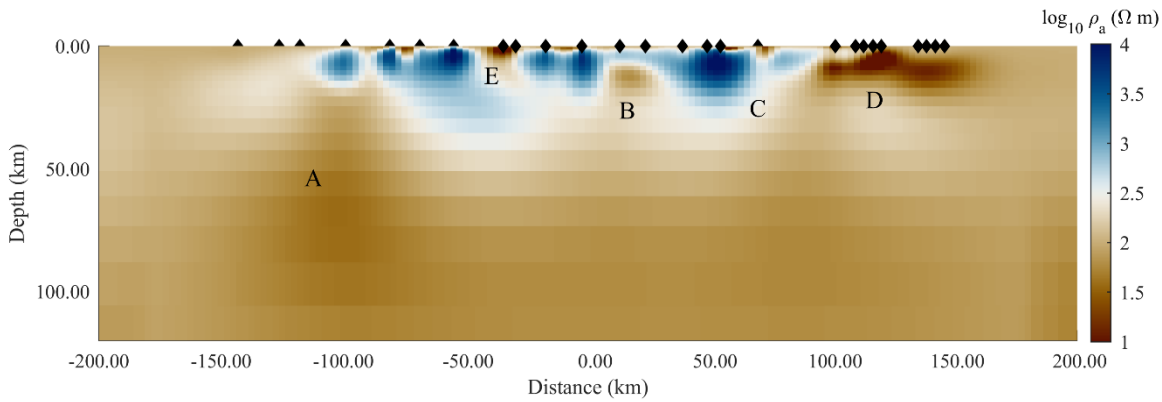


*Figure 13: RMS misfit 1.928354*

I used this model as a starting point to vary parameters in my other models. In this model, important features noted in the region include the large resistive zone between -100 km west and 80 km east, a large conductor in the west extending from 25 km to 120 km in depth (A), and a strongly conductive eastern feature from the surface to 25 km depth (D). Smaller conductive features break up the central resistive region (B, C). These features are constrained in the subsequent models. The west is mostly indistinguishable from the starting resistivity of 100 Ω m and includes a conductor underneath a more resistive block (at a lateral position of -100 km) (A). The model inserts features to a depth of 70 km. This model has the lowest RMS misfit of all models but was not chosen as the final model as other models better matched known geological features in the region (See Model F).

## Model B

Starting Resistivity 10 Ω m and covariance of 0.3

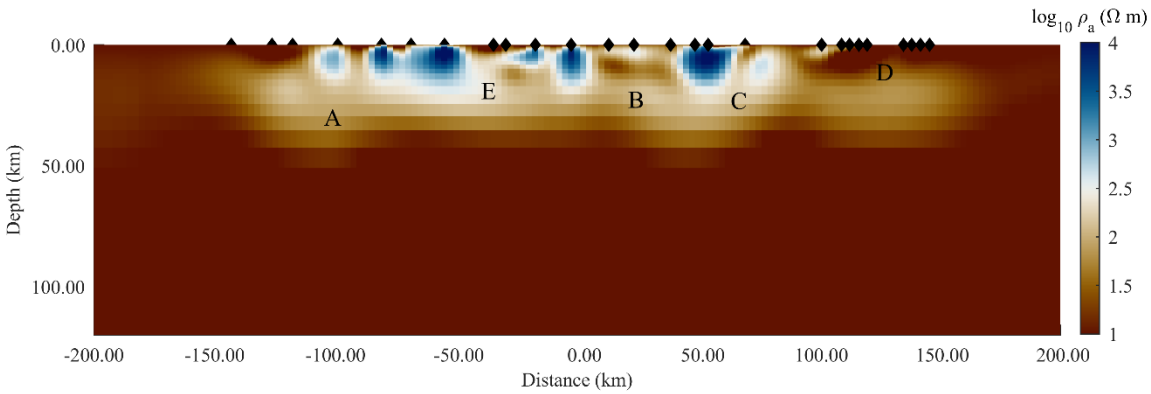


*Figure 14: RMS misfit 1.963777*

In this model, the aim was to use a low resistivity to constrain resistive features. This low resistivity creates a conductive background which the model is forced to deviate from when inverting the data. Features that are strongly resistive will still appear in the model, while features that are more weakly resistive may not. The central resistive region in Model A is still strong. These blocks are surrounded with areas of 500 Ω m. Thus, this region is well constrained. Conductive features are not distinguished from the background resistivity of the model, although the shape of the eastern conductor D is still evident. Features in this model at 0.3 covariance are placed slightly deeper than those of the 0.2 model, although no robust features appear below 50 km.

## Model C

Starting Resistivity 1000 Ω m and covariance of 0.3

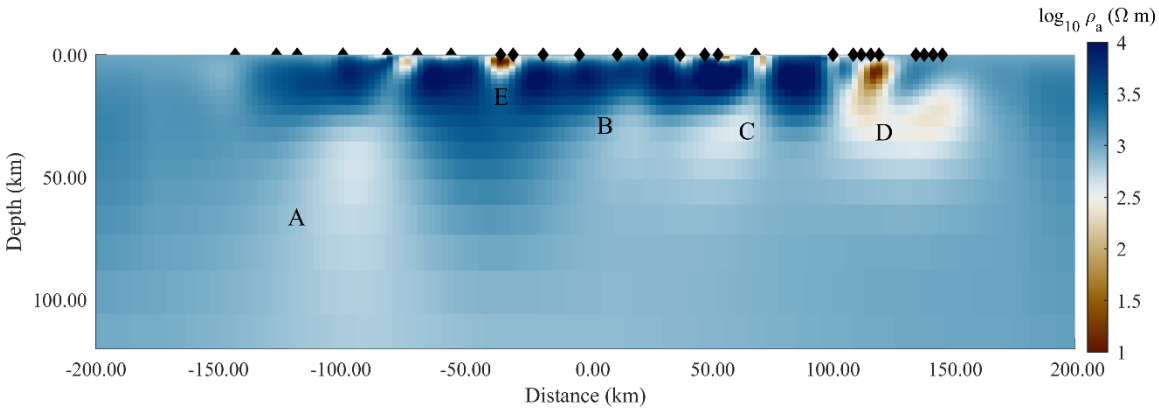


*Figure 15: RMS misfit 2.047308*

This model was used to constrain conductive features in the model and was useful for comparison with the higher covariance models. The RMS misfit on this model is higher than those with a lower

starting resistivity, suggesting that the region on average is less resistive than the starting model. Strong conductive features that appear in the model include: a large conductor at depth (25 km) in the west, several shallow conductors across the resistive central block, two partially conductive regions (10 km and 50 km east of model centre B and C), and a much stronger conductor at 120 km east of the model centre D. The shallow conductors exist in regions where the model has low resolution. The two partially conductive regions are not robust as they appear much stronger in less resistive models. In the covariance 0.3 models A, B and C, it is interesting to note that the larger, less resistive features appear to join up with those that are shallower between the resistive blocks.

### Model D

Starting Resistivity 100 Ω m and covariance of 0.2

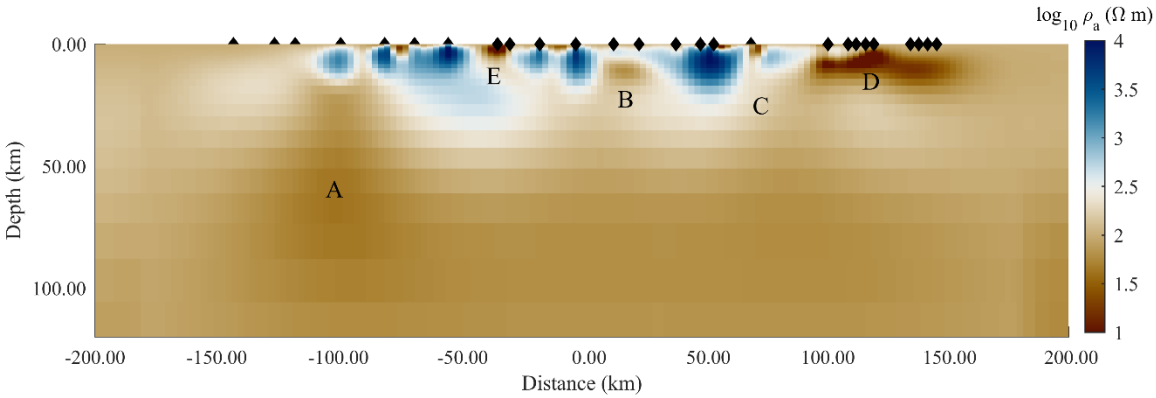


*Figure 16: RMS misfit 2.013814*

The goal of running the inversion with these parameters was to test the fit of the data to stations with a low smoothing factor. The model inserts features shallow in the subsurface and tends to put features close to the individual stations. The features are well defined but do not extend into the subsurface beyond 50 km. Strong features in this model include the resistive blocks in the central region (down to a depth of 20 km) and the large conductor in the east (D). A western conductor (A) at depth is evident and appears below a resistive block. Much of the model at depth blends to the starting resistivity. The model took more iterations to find adequate station fits than the 0.3 (A, B,C) or 0.6 (D, E,F) covariance models.

## Model E

Starting Resistivity 100 Ω m and covariance of 0.6

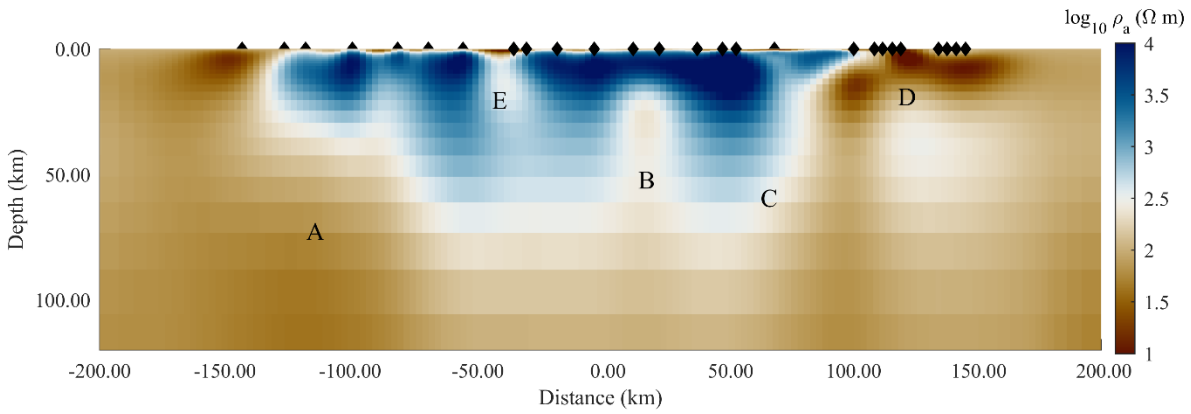


*Figure 17: RMS misfit 2.111788*

This model was run to see the effects of smoothing rugged features in the model. This avoids the interpretation of small features that are not robust. The result is a model which matches more closely to regional geological features, such as the depth to the Moho which is well constrained (Dentith et al., 2000). The base of the strong eastern conductor (D) at 100 km east is slightly deeper at ~ 42 km. A starting resistivity of 100 Ω m was chosen to compare this model with the 0.3 (Model A) and 0.2 (Model D) models. Features are well constrained to 120 km in the subsurface. The resistive block is well defined, and extends between stations, as opposed to the 0.2 and 0.3 covariance models in which the resistors only appear directly under resistive stations. The conductive feature (E) in the west underneath the resistive block (- 120 km west from model centre) is well constrained and less resistive than the initial resistivity. The central resistive region appears to extend deeper in this model than in models A through D. The large eastern conductor (D) is robust and appears connected to conductors that extend into the mantle. The two partially conductive regions (B and C) described in model D are present in this model. The feature at 10 km east is one of these and does not appear to reach the upper crust in this model.

## Model F

Starting resistivity 500 Ω m and covariance of 0.6

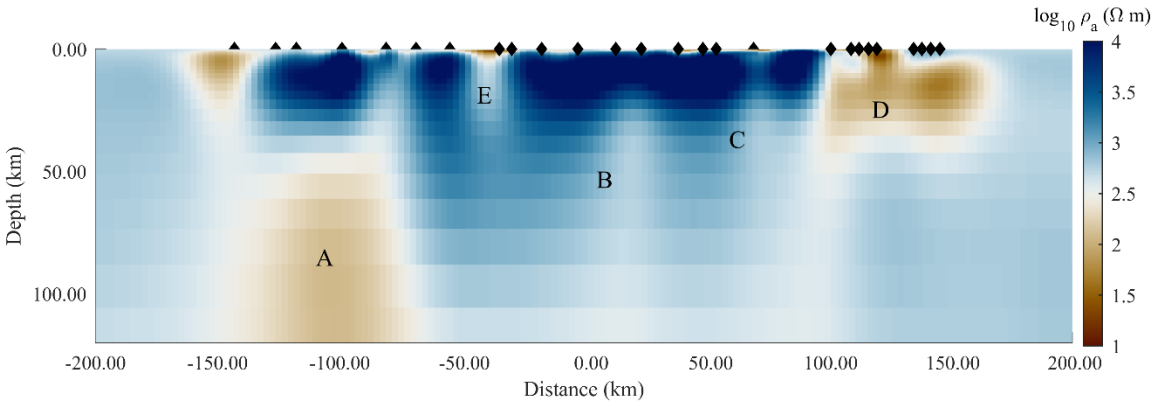


*Figure 18: RMS misfit 2.104472*

Model F was constructed to find a lower RMS misfit than models E and G. Conductive features in this model are robust due to the higher starting resistivity. Features mentioned previously are all present. The resistive block in the centre is well defined and still includes the less resistive regions which divide up the resistive blocks, for example, less resistive features at -40 km west of the model centre. This model had the lowest RMS misfit of the 0.6 covariance models and is used as the final model. The background resistivity of 500 Ω m used in Model F best represents the region as it allows for a deviation by strong conductors, allows for a large resistive central region, and accounts for a much less resistive lower lithosphere.

## Model G

Starting Resistivity 1000 Ω m and covariance of 0.6

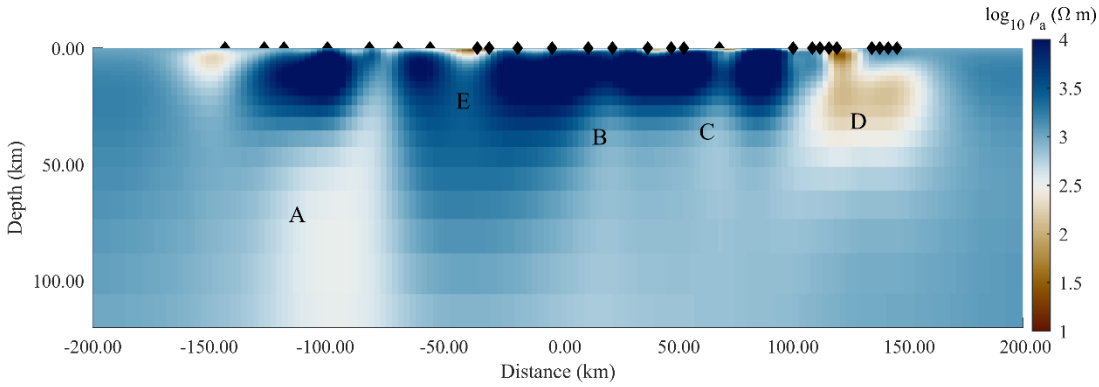


*Figure 19: RMS misfit 2.435089*

Model G was tested to see the effects of the higher covariance and a higher resistivity after success with Model E. This model has the highest RMS misfit of all models. A starting resistivity of 1000 Ω m produced larger misfits across all covariances. This model does not constrain any new features

than previously discussed and is worth noting the most resistive features in the model are in the top 50 km of the model. If the surrounding region is on average less resistive the starting half space, 1000 Ω m will not fit well to the data.

## Model Fits

Model fits plot the apparent resistivity and phase for the initial data set and fit of the models to these data. Model fits were conducted on the Zxx Zxy Zyx and Zyy data outputs from inversion. It was particularly important that the data was fitting at long periods due to the interest in lithospheric structure. There are several important factors in the fit that I looked for in analysis: the fit at long periods, whether the inversion was fitting strong changes in gradient in the initial data, and whether the inversion was fitting Zxx and Zyy well. The fits for changing the covariance and starting resistivities were analysed along with the fit for the final Model F. Even small changes to the RMS misfit in a model are noticeable in the plotted data fits.

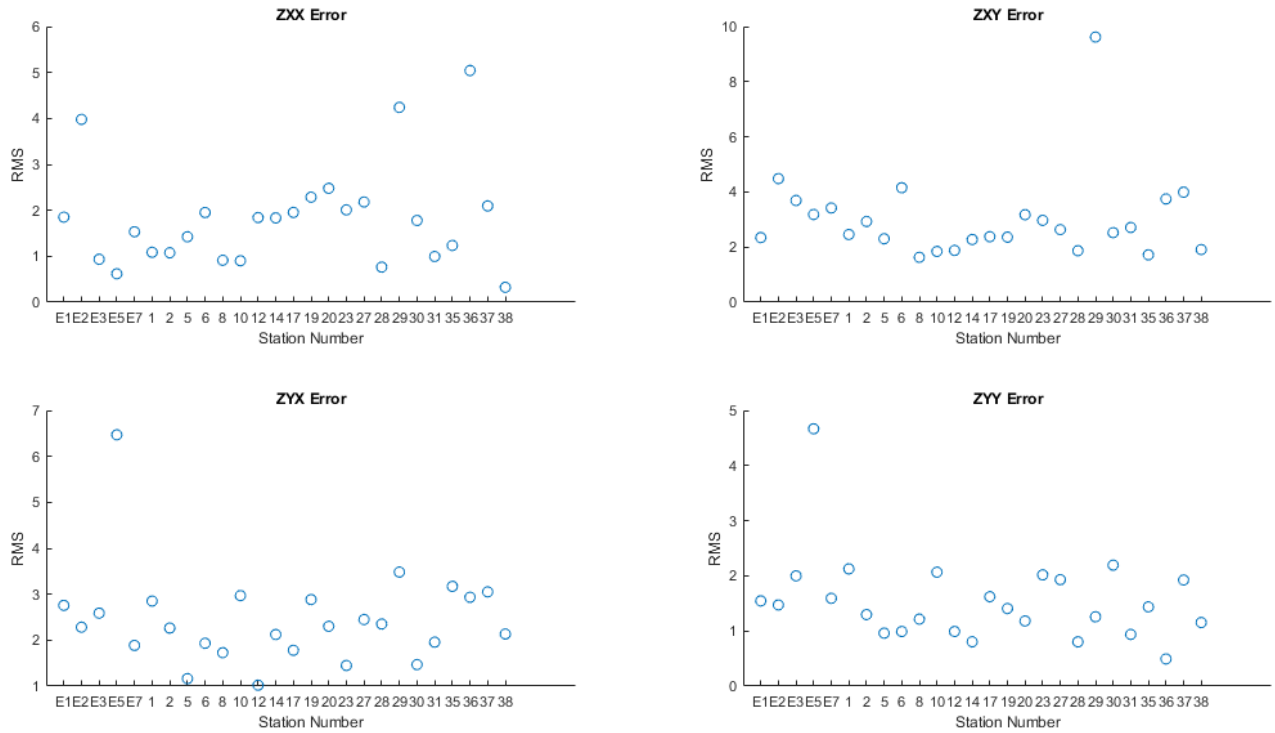


*Figure 20: highlights the RMS Error at each station for all Z components in the final model. The Zxy and Zyx components appear to be raising the overall RMS on the model, along with a few individual stations*

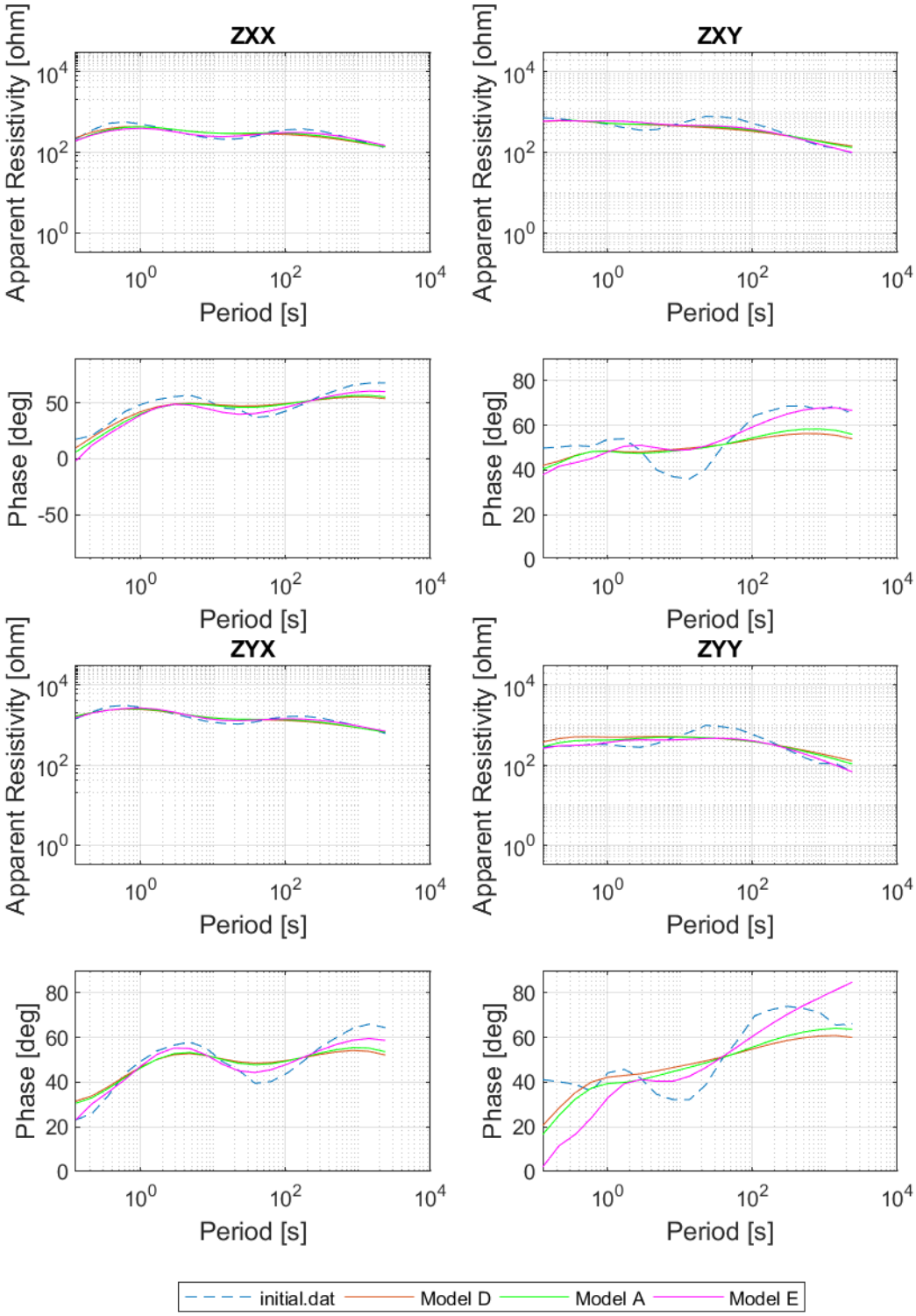


*Figure 21: Model fits for varying covariance at station STYE3. Higher covariance fits rapid changes in of apparent resistivity well, but does not fit the overall magnitude. Model D has covariance 0.2, Modal A 0.3 and Model E 0.6.*

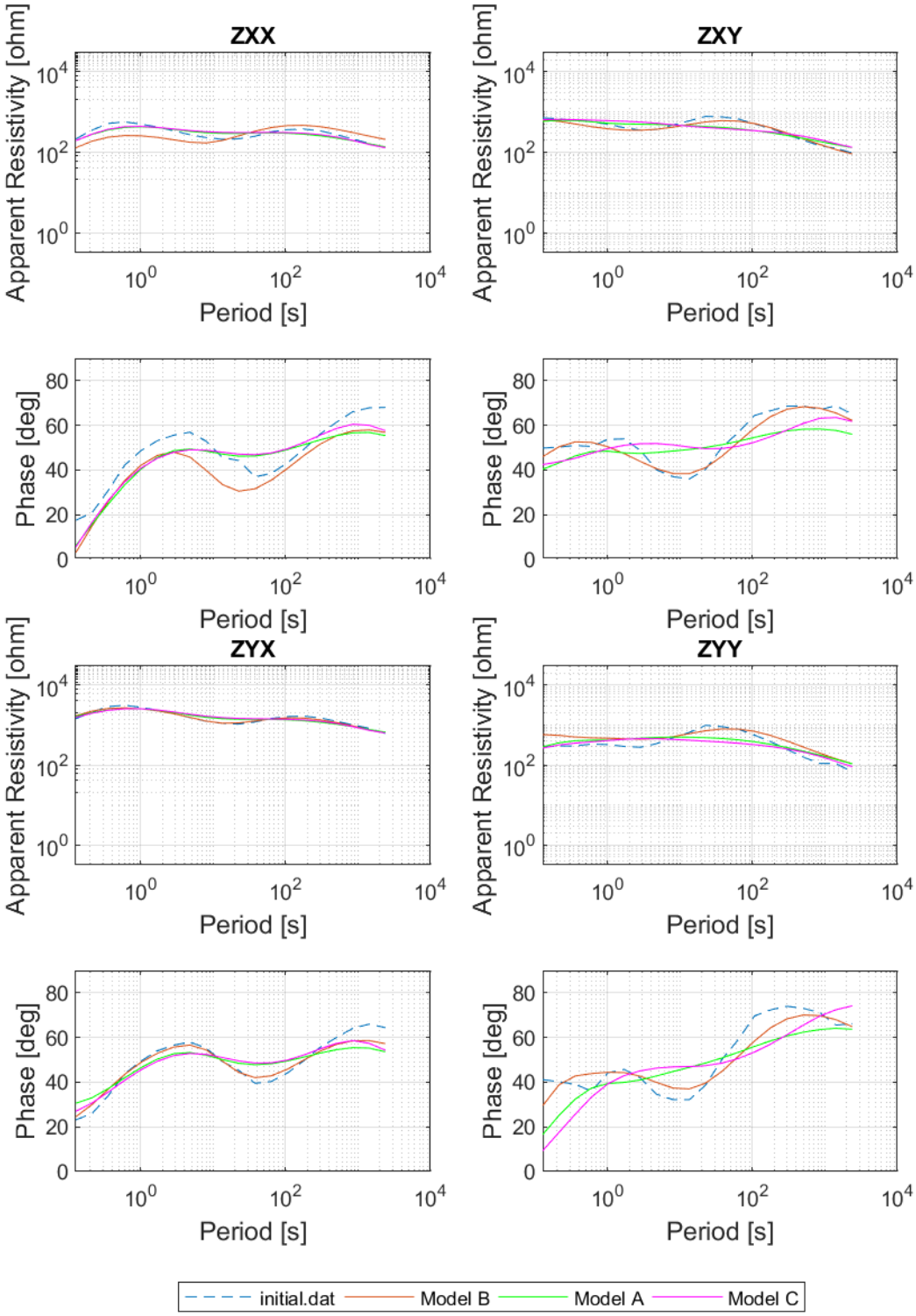


*Figure 22: Model fits for and varying resistivity at station STYE3. High resistivities (1000 Ω m, Model C) do not produce adequate fits compared to moderate (100 Ω m, Model A) and low resistivity (10 Ω m, Model B) starting conditions.*

### Varying covariance

Figure 22, shows fits for three models of varying covariance including Model D (0.2), Model A (0.3) and Model E (0.6). These all had the same starting resistivity of 100 Ω m. The 0.2 and 0.3 covariances fit similarly and in general fit much closer to the initial data than the 0.6 covariance model. The 0.6 Model E had a significantly poorer fit, however often fit better at longer periods than lower covariance models (D, A). The advantage of modelling with a higher covariance is that it was better able to fit strong changes in the shape of the apparent resistivity and phase curves, which were prevalent across the Southern Cross data set.

### Varying resistivity

Figure 22, right, shows fits for models of varying resistivity (Models B, A and C, 10, 100, 1000 Ω m), with a covariance of 0.3. Moderate starting resistivity (100 Ω m) models (A, D and F) fit better than models with a starting resistivity of 1000 Ω m. Similar to the high covariance models, high resistivity starting conditions failed to fit the magnitudes of the apparent resistivity. The RMS misfits also reflected this inability for a high resistivity starting model to fit the data. The starting model of 10 Ω m fit the data very well but is not similar to craton resistivities (highly resistive) and was only used to constrain resistive features in the crust.

### Final model fits

An example of final model fits are shown in Figure 23. The main model used to interpret was Model F, with secondary interpretation from Model A. Model A fit the best out of all inversions attempted. Model F fit better than the other covariance models due to choice in starting resistivity at 500 Ω m. Despite a worse fit than several other models (A, B, C and D), Model F was chosen for final interpretation. The reasoning for this is detailed in section Final Model Choice below.

In general, the fits show that the two models fit the long periods of the initial data set well. Model F is often a better fit in Zxx and Zyy at long periods. Fits across the South West Terrane stations (STYE1 – STY2) are generally good. Typical of the entire survey, the inversion does not fit variation in the data, and instead smooths over the curves. Zxy in Figure 23 is an example of this poor fit. This is observed for all model fits and its cause is unknown. Zxx and Zyy were increasingly poorly fit beneath the Kalgoorlie Terrane and are a source in raising the RMS misfit of the model. Across the central region of the survey (Youanmi Terrane) the Zxy and Zyx data fit well.

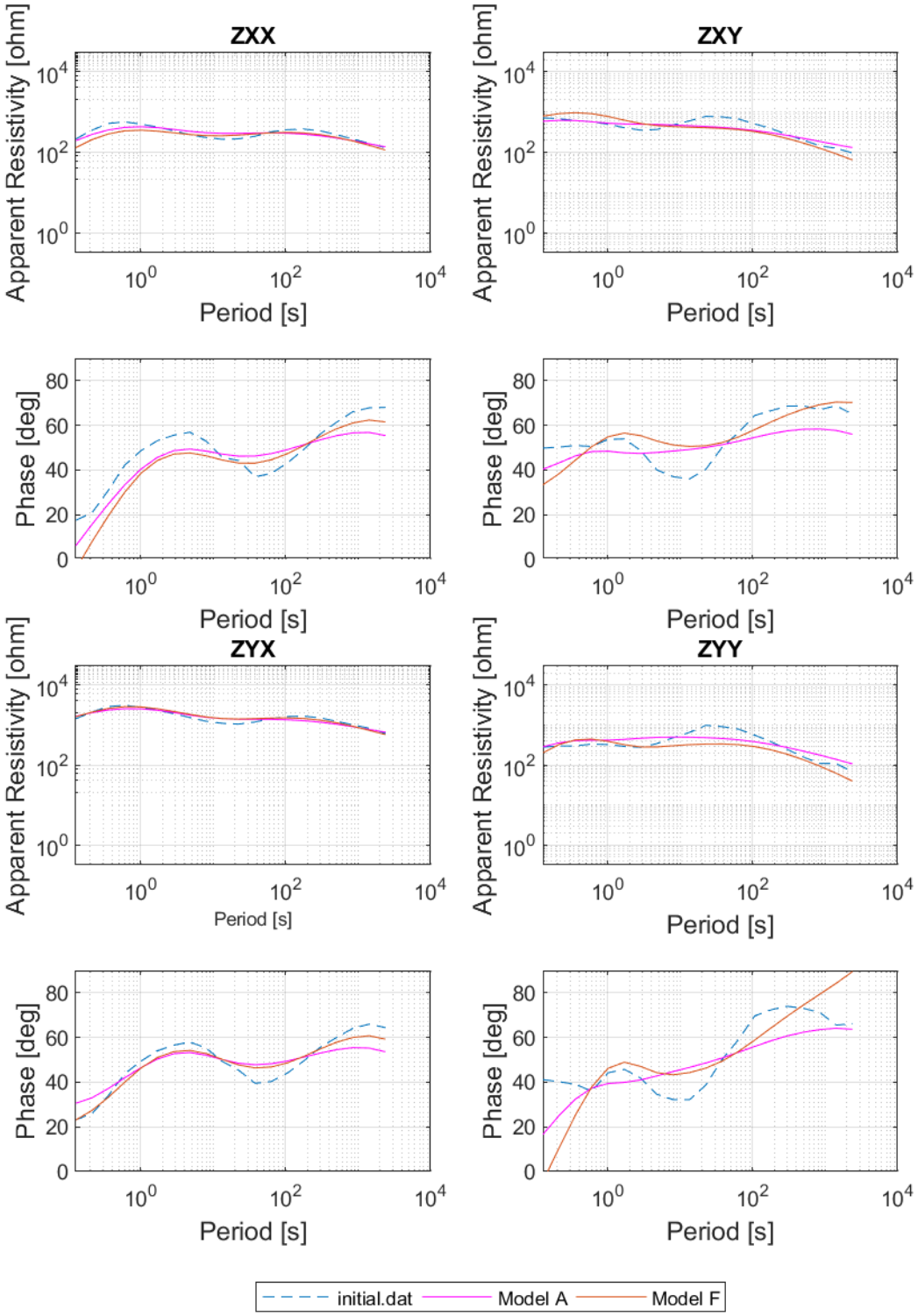


*Figure 23: Model Fits for the final two models Model A (100 Ω m, 0.3 covariance) and Model F (500 Ω m, 0.6 covariance). Model fits for the each station can be found in the supplementary material.*

## Final Model

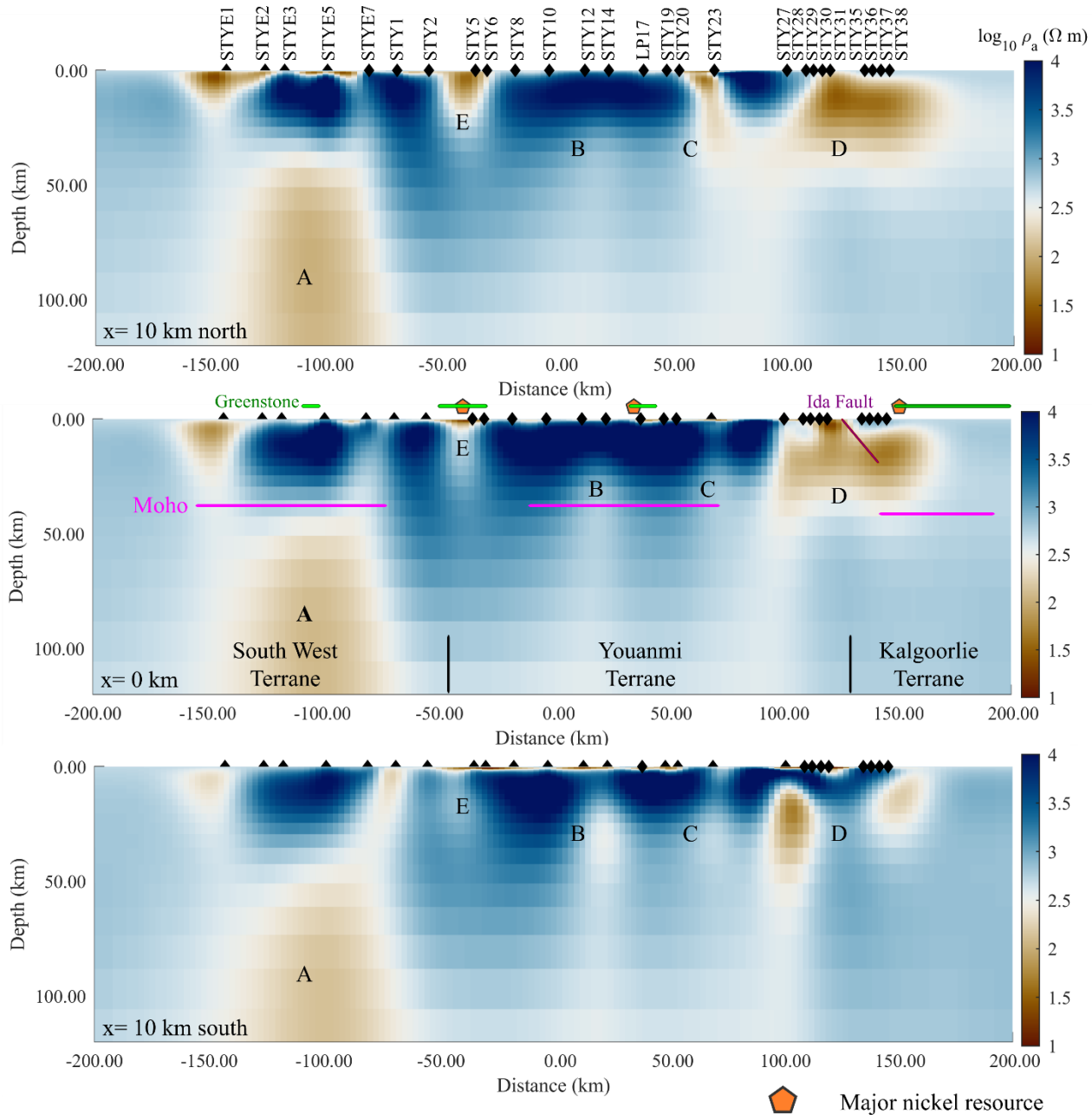


*Figure 24: Three X slices of the final Model F including X = 0, X =10 km north of the survey and X=10 km south. Diamonds are stations in front of the slice and triangles are stations behind the slice. Large conductive features are marked A through E. For the centre profile, domain boundaries, greenstones and major nickel mineral deposits approximate locations have been marked.*

### Final model choice

Model F was chosen as the final model for interpretation. The majority of the inversions (see model A through D) put features at much shallower depths than the 0.6 covariance models (E, F and G). This is in contrast to the depths expected from the period ranges in the data. It is not clear why this is, but this feature has been observed in other data sets modelled with ModEM (Robertson et al., 2018). The higher covariance models seem preferable as they place features at more reasonable

depths. In Model F, conductive features A and D are bounded at a similar depth as the well constrained eastern dipping Moho. Resistive models also increase the depth of features but have high RMS misfits. Model F's 500 Ω m starting resistivity is a good compromise between a strong model fit and reasonable depths for model features.

### Model features

Conductor A is a large conductor in the west (-110 km west of model centre) sitting underneath a resistive block at just under 40 km depth. It extends through the lithosphere to beyond where the model appears to lose resolution at ~120 km. Conductor A extends outwards from the survey in both north and south directions. In the northern part of the survey it appears to connect to a conductor at the western most edge of the survey and also connects to a conductive regions near the surface between STYE5 and STY1. I am unable to comment on these shallow conductors due to low resolution in the top few kilometres.

The central resistive region is a block of high resistivity which extends to a depth of 80 km and possibly deeper. The most resistive part of the region (~8000 Ω m) is in the top 40 km and is broken up by less resistive lithosphere.

Conductor D is a large conductor in the east that extends down to ~40 km. It is three dimensional in nature and appears larger in the northern and centre X slices. It appears as two conductive regions in the southern slice. It may have low resolution underneath it due to attenuation of the electromagnetic signal by the conductor. It appears to connect to the structure marked as C and the less resistive region between the two conductors extends past 120 km.

Conductor B is a less well constrained conductor that is difficult to see in the more resistive models. In Model F it does not appear to reach the surface and is strongest in the southern slice of the model. This feature is particularly strong in models A and E which have a lower starting resistivity.

Conductor C appears to be connected to the large eastern conductor in the northern slice, and while it appears well constrained in models A – D this is in shallow regions with low resolution. This conductor appears strongly in the crust and is less robust below the Moho.

Conductor E is mainly a surface feature, however in the northern slice it runs deeper into the crust. Less conductive regions surround it and extend somewhat below the most resistive sections of the central resistive regions.

## Modelling revision

Revision of this thesis found that the rotation performed on the mesh for inversion did not also rotate the data. A second model was run without rotation using the same initial conditions as Model F. These include a starting resistivity of 500 Ω m and covariance of 0.6. Major features in Model F are also apparent in the revised model, however differ somewhat in shape. The overall RMS error for the revised model increased by 0.3.

Conductor A differs significantly in shape in the revised model. The conductor appears much shallower in the subsurface without a large resistive region above it and is more elongated than in Model F. The central resistive region spans the model and still terminates at the depth of the Moho (42 – 38 km). The resistive blocks appear strongest underneath station locations as in the rotated model. Conductor D loses definition and is modelled spherically, however remains a strong conductor in the east, terminating approximately at the Moho. Conductor B is less resistive in the revised model and is connected to apparent surface features. Conductor C is more resistive in the revised model and however its location remains unchanged. Conductor E is prominent in the revised model and least resistive 10 km north of the east west slice of the survey.

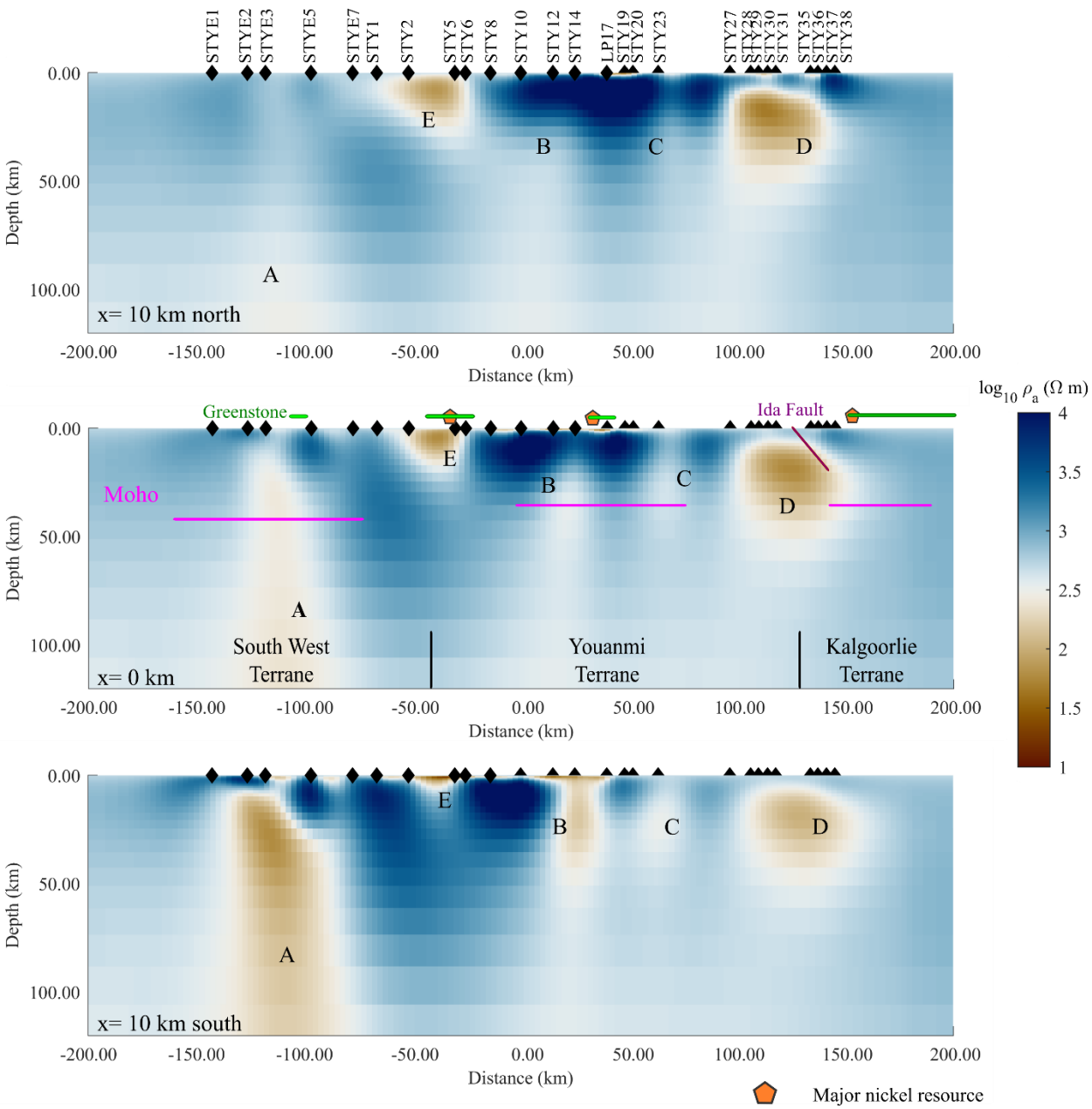


*Figure 25: Revised un-rotated final model F. Major features occur in the same locations however differ slightly in shape and resistivity. Final RMS Error of 2.405829*

# Discussion

## Conductor A

Conductor A is a large conductive 3D region in stark contrast to a resistive block above it. It extends from a depth of approximately 35 km to a depth of approximately 120 km and appears to connect to the crust east of the main conductive body. The 'top' of conductor A is also the depth to the Moho in the south west of the Yilgarn Craton as defined by seismic data (Dentith et al., 2000). This similarity to the position of the Moho was one purpose in choosing a 0.6 covariance as the most reasonable for use in interpretation, as these features match geologically. Results from the revised un-rotated model include Conductor A extending from 10 km depth to 120 km depth. This does not validate the use of the 0.6 starting model. The difference between the conductivity of conductor A and the overlying resistivity at the base of the crust is strong and suggests a change in composition. This difference may be related to mafic underplating, where material from the mantle 'ponds' at the base of the crust (Thybo & Artemieva, 2013). Underplating has also been suggested as a mechanism for the high velocity zone mapped at the base of the crust in Corrigin, 50 km from the western edge of the Southern Cross MT Survey (Dentith et al., 2000).

The composition difference between conductor A and the surrounding resistive region can be explained by an introduction of enriched mantle material into the lithosphere. Conductor A is likely a geochemically enriched region. However since there is no komatiite mineralisation in the South West Terrane, this large conductor is unlikely to be related to the nickel deposits found in the Youanmi and Kalgoorlie terranes. It may be related to gold mineralisation which occurs throughout the Yilgarn craton, occurring just before cratonization.

This survey was the first to obtain MT data in the South West Terrane. Additionally, there is little sensitivity in the model to the west of Conductor A, as it is right on the edge of the survey, so I cannot determine if it represents a single mantle feature, or the conductivity typical of the South West Terrane. The eastern region of the South West Terrane has comparatively less mineralisation than the Youanmi and Kalgoorlie terranes (Witt & Vanderhor, 1998) so it is possible that enriched mantle has not focussed into the upper crust to form mineralised regions and instead sits in the lithosphere. Cratonic lithospheres are not expected to have an enriched composition, (Griffin et al., 2009) so it is unlikely that Conductor A is indicative of South West Terrane lithospheric resistivity.

### Central Resistive Region

The central resistive region extends across much of the survey subsurface crossing all of the Youanmi Terrane and extends approximately 100 km into the South West Terrane. This region is characteristic of Archean cratons as described above, with its most resistive features modelled at 8,000 Ω m. It is interesting to note that several shallow conductors align geologically with the greenstone units (and their mineralisation) in the region, however, since resolution is poor in the uppermost few kilometres, I cannot comment on this at length. There are only two long period stations inside the resistive region which are STY6 and STY17. This long period information contributes to the resolution of the depth of the resistive block at more than 120 km. In these highly resistive regions, there is a much deeper sensitivity in the model, and thus features can be interpreted at depth. Interestingly the Youanmi (YU2) MT traverse conducted parallel in the northern Youanmi terrane highlights a similar central resistive block, which extends to the Moho (Milligan, 2013). This comparison of MT data corroborates the seismic and geochemical evidence used to justify the combination of the Murchison and Southern Cross domains as one terrane (Champion & Cassidy, 2007).

### Conductors B and C

The less resistive regions at 10 (B) and 100 km (C) east of the centre of the profile are weakly constrained and may occur due to a lack of long period information in this region. More long period data would help to characterise the depth and structure of these less resistive features. These features shift in position depending on the covariance and starting resistivity of the model. Feature B is the best constrained and occurs close to 10 km east in almost all model variations, while Feature C appears either underneath the large conductor D or at 50 km into the model as in Model F. In the revised un-rotated model, Feature B has a much lower conductivity, and appears to be connected to a surface feature. These features could possibly be related to a komatiite mineralisation event. Conductor B occurs several kilometres to the west of the Emily Ann and Maggie Hays nickel sulphide deposits which are hosted in komatiite (Hoatson et al., 2006). The low resistivity models do not strongly constrain the resistivity above the less resistive Conductor B. As the model resolves a direct pathway, it is possible that Conductor B could be associated with this mineralisation. This mineralisation may have occurred during the focussing of a mantle plume along a west dipping subducting slab at 2715 – 2690 Ma (Czarnota et al., 2010; Mole et al., 2015). This could have mineralised the conductive regions below the Forrestania and Southern Cross greenstone belts nickel deposits. The higher resistivity than Conductors A and D may be due to reworking of the crust and mantle events post komatiite introduction.

## Conductor D

Conductor D is a large robust conductive feature appearing in every model. The conductor is well constrained to a depth of approximately 30 km. Underneath this, some models show a continuing conductive feature connecting to Conductor C and other models show a lithosphere that blends into the initial model resistivity. This could be due to the nature of MT modelling which is better at resolving conductors than resistors. Figure 26 is a perpendicular slice of the conductor. The phase tensor information for this feature is in **Error! Reference source not found.**. At all periods the d irection of the strike is inconsistent, however only at periods of 90 s or less is there a high ellipticity indicating a complex structure that becomes less complex at depth. Due to being a conductive region, the longer periods in the phase tensor data in the east are likely displaying shallower information than those phase tensors in the west. The phase tensors at longer periods have a much lower ellipticity which does not occur across the rest of the survey. This suggests that the structure at the base of Conductor D is either less complex than the rest of the region, or less well constrained.

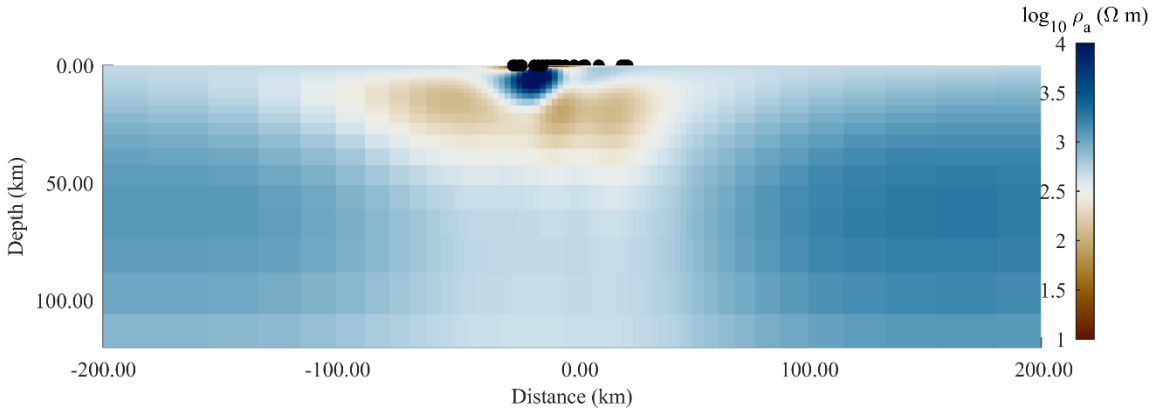


*Figure 26: Y slice of Model F at +110 east of the model centre examining conductor D. This feature is three dimensional and exists either side of a resistive block. This could explain why the phase tensors in the region vary so much between nearby stations.*

The conductor could be linked with all the other less resistive regions in the survey as part of the large mineralisation event which emplaced the komatiites in the region. This conductor is also placed similarly close to a large nickel deposit as with the other discussed conductors, however this nickel deposit occurs in the Kalgoorlie Terrane. If Conductor D formed by a mantle anomaly during subduction and compression, then the focussing of the mantle fluids would have been in a shallower region due to the subducting plate being closer to the crust at this location. This could have resulted in the shallower and more strongly conducting feature seen in Conductor D compared to conductors B and C.

The previous MT survey from the EGF01 line in the north found the Kalgoorlie region to be overall less resistive than the adjacent Youanmi and Kurnalpi terranes (Czarnota et al., 2008). This is also seen in our survey however, it is difficult to compare with the model from the Southern Cross as Conductor D spans the Kalgoorlie Terrane. The Ida Fault which separates the two terranes is likely not imaged by this survey, as there is no striking contrast in conductivity where the fault is located. Czarnota et. al. (2008) also conclude that they are unable to map the Ida Fault in the EGF01 MT (Blewett et al., 2010; Czarnota et al., 2008). Conductor D occurs on the footwall of the Ida Fault, rather than the hanging wall, which is unexpected for the resistive Youanmi Terrane. The conductive region may be consistent with the mineralisation of the Kalgoorlie terrane.

Sm Nd isotopic data in Figure 1 show a clear distinction between the EGST and the Youanmi and South West Terranes. The geochemical isotopic data model the younger region of crust slightly west of the Ida Fault in the survey region (Figure 1). It is clear that Conductor D is placed at the limits of the conductive region and the surface directly above the conductor better matches the model ages for the Kalgoorlie Terrane. Two mantle plume events have been suggested for emplacing komatiites in the region. These occurred in the Kalgoorlie Terrane at approximately 2.7 Ga and in the Youanmi Terrane at 2.9 Ga (Mole et al., 2015). Conductor D may have formed at a similar time to the Kalgoorlie Komatiites, as opposed to with the Youanmi Komatiites.

If this conductor is unrelated to komatiite emplacement in the region, it may possibly be associated with orogenic gold events which mineralised the crust in the Kalgoorlie region. This mineral emplacement occurred just prior to cratonization, and is a possible explanation for why it occurs on the footwall of the Ida Fault (Czarnota et al., 2010). Additionally, Conductor D would not be associated with the gold directly, but rather an enriched mantle and lower crust associated with the mineralisation event.

### Conductor E

Conductor E is much more conductive in the 10 km north survey slice crossing stations STY2 and STY5. Interpretation of the uppermost few kilometres is not possible, however it is useful to note the Youanmi greenstone belt is directly above this location, and hosts the large Flying Fox and Good Morning nickel deposits. Figure 9 shows the proximity of STY5 to these deposits. The surrounding resistive blocks are broken up by a less resistive pathway 10 km to the west of conductor E. It is possible that these less resistive regions could be pathways for mineralisation from conductor A to conductor E. Similarly, station LP17 is co-located with the Emily Ann Nickel deposit, and although we these features are not resolved at such shallow depths, it is possible that Conductors B and C are related to this mineralisation.

### What MT does not delineate

The models generated in this thesis do not provide good resolution of structures below 120 km and as such do not image the base of the lithosphere, which is expected to be at 200 km depth (A. M. Reading et al., 2003). MT has been unable to identify large faults such as the Ida Fault and Youanmi Faults in this region. Due to low resolution in the upper few kilometres other fault and shear zone structures (Koolyanobbing Shear Zone) are either not imaged or interpreted here. The horizontal high velocity body which is ~70 km deep in the west and 120 km deep under the Ida Fault, is also not likely visible in the MT analysis.

## Comparison to Dentith et al 2013

The 2-D model shares several major features with the 3-D model. Figure 27 offers a comparison between the Dentith et al. (2013) model and my revised un-rotated model. The 2-D model is characterised by a strongly resistive upper crust which is also present in the 3-D model. This crustal feature is broken up by less resistive areas across both models. Conductor D is present in both models, however these regions are different in shape and depth. This conductor in the 3-D model is shallower in the subsurface at just 5 – 10 km depth. Conductor D is intersected by the Moho in both models.

Conductor A is not present in the 2-D model. In the 2-D model a region of high resistivity is present in the same location labelled 'N'. Dentith et al. (Dentith et al., 2013)states that there may not be good resolution in the model at this depth. Conductors B and C (3-D model) see similar regions of resistivity in the 2-D model, however all conductors connecting to a central less resistive unit in the lower crust is not apparent in the 3-D model. In the 3-D model, less resistive regions extend to the model limits. The units interpreted over the 2-D model could be broadly applicable also to the 3-D model, and are offset from the determined terrane boundaries. 'Unit 3' is drawn to the left of the eastern conductive region, while the boundary between Units 1 and 2 is drawn at the edge of feature N. In the 3-D model this could be placed between Conductor A and the central resistive region. As there is weak resolution in the 3-D model for the upper crust, strong comparisons are avoided.

While major features occur in both models, each inversion process produces a model which is significantly different in the shapes of these features. The final 3-D model highlights how some features (conductors B, D and E) change in three dimensions and are best represented by a 3-D inversion.

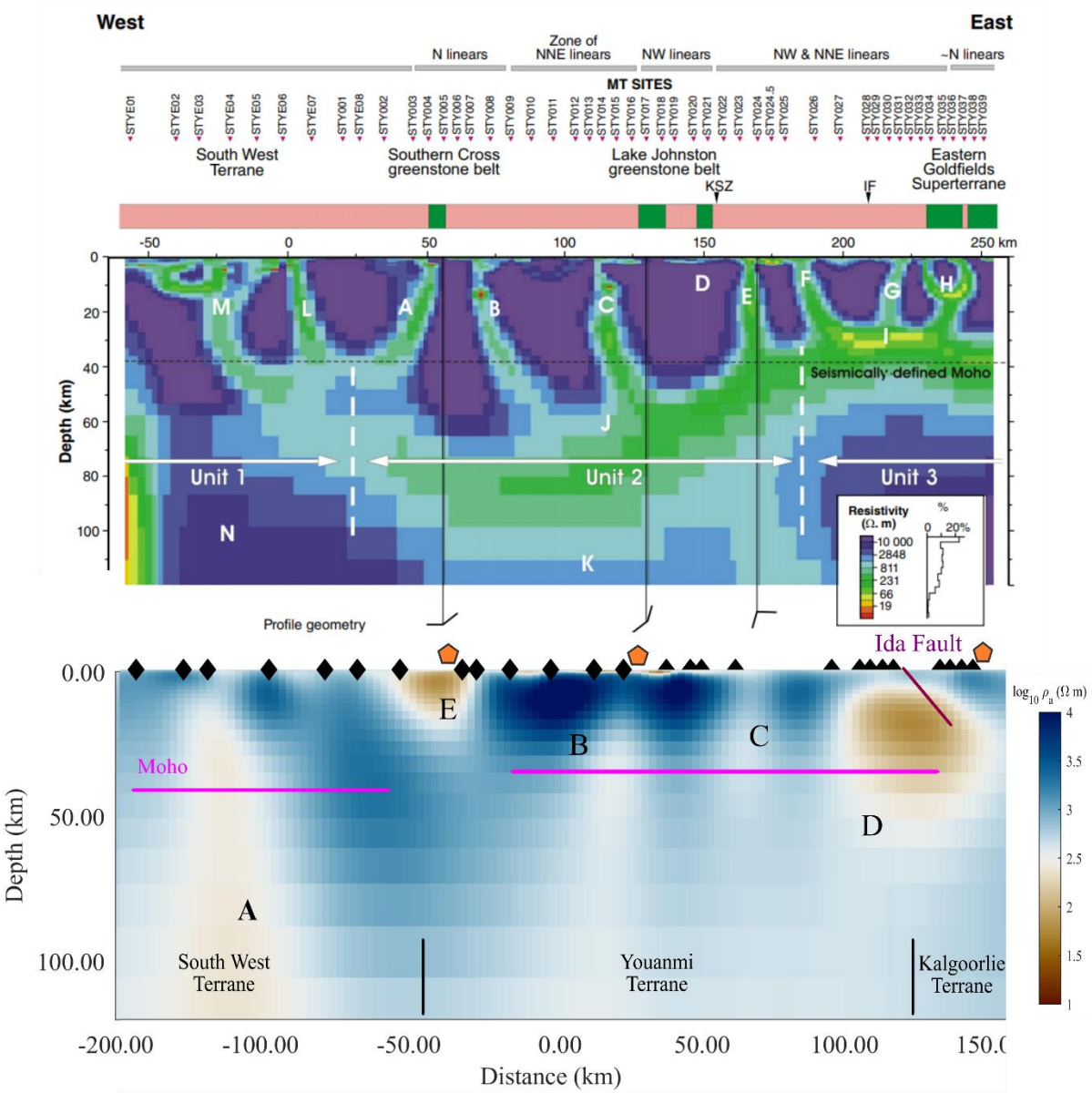


*Figure 27: Comparison of the two dimensional vs three dimensional results with the Dentith Data set. This figure is adapted from* (Dentith et al., 2013).

# Conclusions

The lithosphere beneath the South West, Youanmi and Kalgoorlie Terranes was examined in this thesis through the 3D inversion of magnetotelluric data.

- Data were obtainable from long period data sets and contributed to the resolution of the model at depth.
- Phase tensor analysis identified areas of complexity in the lithosphere, requiring 3D inversion of this data.
- Modelling found the region is best represented with a high covariance of 0.6 and a moderate resistivity of 500 Ω m.
- Several large conductive features are present and may be related to mineral emplacement of komatiites in the region, or mantle enrichment related to gold mineralisation.

Future work in the region would benefit from geophysical data collection in the Youanmi Terrane between the Southern Cross MT survey and the EGF01 seismic and MT lines. Constraining the location of the Ida Fault in the southern Youanmi Terrane would benefit the delineation of the Terrane boundary between the Youanmi and Kalgoorlie terranes, and aid in further interpretation of conductors in the region.

## References


Anand, R. R., & Paine, M. (2002). Regolith geology of the Yilgarn Craton, Western Australia: Implications for exploration. *Australian Journal of Earth Sciences*, *49*(1), 3–143. https://doi.org/10.1046/j.1440-0952.2002.00912.x

Arndt, N. (2003). Komatiites, kimberlites, and boninites. *Journal of Geophysical Research: Solid Earth*, *108*(B6). https://doi.org/10.1029/2002JB002157

Barley, M. E., & Groves, D. I. (1990). Deciphering the tectonic evolution of Archaean greenstone belts: the importance of contrasting histories to the distribution of mineralization in the Yilgarn Craton, Western Australia. *Precambrian Research*, *46*(1–2), 3–20. https://doi.org/10.1016/0301-9268(90)90064-W

Barley, M. E., Brown, S. J. A., Krapež, B., & Kositcin, N. (2008). Physical volcanology and geochemistry of a Late Archaean volcanic arc: Kurnalpi and Gindalbie Terranes, Eastern Goldfields Superterrane, Western Australia. *Precambrian Research*, *161*(1–2), 53–76. https://doi.org/10.1016/j.precamres.2007.06.019

Barley, M. E., Kerrich, R., Reudavy, I., & Xie, Q. (2000). Late Archaean Ti-rich, Al-depleted komatiites and komatiitic volcaniclastic rocks from the Murchison Terrane in Western Australia. *Australian Journal of Earth Sciences*, *47*(5), 873–883. https://doi.org/10.1046/j.1440-0952.2000.00820.x

Barnes, S. J. (2006). Komatiite-hosted nickel sulfide deposits: geology, geochemistry, and genesis. *Society of Economic Geologists Special Publication*, *13*, 51–118.

Barnicoat, A. C., Fare, R. J., Groves, D. I., & McNaughton, N. J. (1991). Synmetamorphic lode-gold deposits in high-grade Archean settings. *Geology*, *19*(9), 921–924. https://doi.org/10.1130/0091-7613(1991)019<0921:SLGDIH>2.3.CO;2

Bibby, H. M., Caldwell, T. G., & Brown, C. (2005). Determinable and non-determinable parameters of galvanic distortion in magnetotellurics. *Geophysical Journal International*, *163*(3), 915–930. https://doi.org/10.1111/j.1365-246X.2005.02779.x

Blewett, R. S., Henson, P. A., Roy, I. G., Champion, D. C., & Cassidy, K. F. (2010). Scale-integrated architecture of a world-class gold mineral system: The Archaean eastern Yilgarn Craton, Western Australia. *Precambrian Research*, *183*(2), 230–250. https://doi.org/10.1016/j.precamres.2010.06.004

Blewett, R. S., Czarnota, K., & Henson, P. A. (2010). Structural-event framework for the eastern Yilgarn Craton, Western Australia, and its implications for orogenic gold. *Precambrian Research*, *183*(2), 203–229. https://doi.org/10.1016/j.precamres.2010.04.004

Booker, J. R. (2014). The Magnetotelluric Phase Tensor: A Critical Review. *Surveys in Geophysics*, *35*(1), 7–40. https://doi.org/10.1007/s10712-013-9234-2

Cagniard, L. (1953). Basic Theory of the Magneto Telluric Method of Geophysical Prospecting. *Currents*, *Geophysics*(18), 605–635.

Caldwell, T. G., Bibby, H. M., & Brown, C. (2004). The magnetotelluric phase tensor. *Geophysical Journal International*, *158*(2), 457–469. https://doi.org/10.1111/j.1365-246X.2004.02281.x

Campbell, I. H., Griffiths, R. W., & Hill, R. I. (1989). Melting in an Archaean mantle plume: Heads it's basalts, tails it's komatiites. *Nature*, *339*(6227), 697–699. https://doi.org/10.1038/339697a0

Champion, D. C., & Cassidy, K. F. (2007). An overview of the Yilgarn craton and its crustal

evolution. *Proceedings of Geoconferences (WA) Inc., Kalgoorlie '07 Conference*, 8–12.

Czarnota, K., Champion, D. C., Goscombe, B., Blewett, R. S., Henson1, P. A., P.B., … Groenewald, B. (2008). *Concepts to targets : a scale - integrated mineral systems study of the Eastern Yilgarn Craton Compiled by the Y4 Project Team*.

Czarnota, K., Champion, D. C., Goscombe, B., Blewett, R. S., Cassidy, K. F., Henson, P. A., & Groenewald, P. B. (2010). Geodynamics of the eastern Yilgarn Craton. *Precambrian Research*, *183*(2), 175–202. https://doi.org/10.1016/j.precamres.2010.08.004

Dentith, M. C., Dent, V. F., & Drummond, B. J. (2000). Deep crustal structure in the southwestern Yilgarn Craton, Western Australia. *Tectonophysics*, *325*(3–4), 227–255. https://doi.org/10.1016/S0040-1951(00)00119-0

Dentith, M. C., Evans, S., Thiel, S., Gallardo, L., Joly, A., & Romano, S. S. (2013). *A magnetotelluric traverse across the southern Yilgarn Craton*.

Egbert, G. D. (1997). Robust multiple-station magnetotelluric data processing. *Geophysical Journal International*, *130*(2), 475–496. https://doi.org/10.1111/j.1365-246X.1997.tb05663.x

Egbert, G. D., & Kelbert, A. (2012). Computational recipes for electromagnetic inverse problems. *Geophysical Journal International*, *189*(1), 251–267. https://doi.org/10.1111/j.1365-246X.2011.05347.x

Fishwick, S., & Rawlinson, N. (2012). 3-D structure of the Australian lithosphere from evolving seismic datasets. *Australian Journal of Earth Sciences*, *59*(6), 809–826. https://doi.org/10.1080/08120099.2012.702319

Fishwick, S., & Reading, A. M. (2008). Anomalous lithosphere beneath the Proterozoic of western and central Australia: A record of continental collision and intraplate deformation? *Precambrian Research*, *166*(1–4), 111–121. https://doi.org/10.1016/j.precamres.2007.04.026

Fishwick, S., Kennett, B. L. N., & Reading, A. M. (2005). Contrasts in lithospheric structure within the Australian craton - Insights from surface wave tomography. *Earth and Planetary Science Letters*, *231*(3–4), 163–176. https://doi.org/10.1016/j.epsl.2005.01.009

Gamble, T. D., Goubau, W. M., & Clarke, J. (1979). Magnetotellurics with a remote magnetic reference. *Geophysics*, *44*(1), 53–68. https://doi.org/10.1190/1.1440923

Goleby, B. R., Blewett, R. S., Fomin, T., Fishwick, S., Reading, A. M., Henson, P. A., … Nicoll, M. (2006). An integrated multi-scale 3D seismic model of the Archaean Yilgarn Craton, Australia. *Tectonophysics*, *420*(1–2), 75–90. https://doi.org/10.1016/j.tecto.2006.01.028

Griffin, W. L., O'Reilly, S. Y., Afonso, J. C., & Begg, G. C. (2009). The composition and evolution of lithospheric mantle: A re-evaluation and its tectonic implications. *Journal of Petrology*, *50*(7), 1185–1204. https://doi.org/10.1093/petrology/egn033

Griffin, W. L., Begg, G. C., & O'Reilly, S. Y. (2013). Continental-root control on the genesis of magmatic ore deposits. *Nature Geoscience*, *6*(11), 905–910. https://doi.org/10.1038/ngeo1954

Heinson, G., Didana, Y., Soeffky, P., Thiel, S., & Wise, T. (2018). The crustal geophysical signature of a world-class magmatic mineral system. *Scientific Reports*, *8*(1). https://doi.org/10.1038/s41598-018-29016-2

Henson, P.A., Blewett, R. S. (2006). *Metal transport and depositional processes. In: Blewett, R.S., Hitchman, A.P. (Eds.), Final Report, 3D Geological Models of the Eastern Yilgarn Craton*.

Hoatson, D. M., Jaireth, S., & Jaques, A. L. (2006). Nickel sulfide deposits in Australia: Characteristics, resources, and potential. *Ore Geology Reviews*.

https://doi.org/10.1016/j.oregeorev.2006.05.002

Jones, A. G., Lezaeta, P., Ferguson, I. J., Chave, A. D., Evans, R. L., Garcia, X., & Spratt, J. (2003). The electrical structure of the Slave craton. *Lithos*, *71*(2–4), 505–527. https://doi.org/10.1016/j.lithos.2003.08.001

Kelbert, A., Meqbel, N., Egbert, G. D., & Tandon, K. (2014). ModEM: A modular system for inversion of electromagnetic geophysical data. *Computers and Geosciences*, *66*, 40–53. https://doi.org/10.1016/j.cageo.2014.01.010

Leary, P., & Phinney, R. A. (1974). A magnetotelluric traverse across the Yellowstone Region. *Geophysical Research Letters*, *1*(6), 265–268. https://doi.org/10.1029/GL001i006p00265

Ledo, J. (2005). 2-D versus 3-D magnetotelluric data interpretation. *Surveys in Geophysics*, *26*(5), 511–543. https://doi.org/10.1007/s10712-005-1757-8

Livelybrooks, D., Mareschal, M., Blais, E., & Smith, J. T. (1996). Magnetotelluric delineation of the Trillabelle massive sulfide body in Sudbury, Ontario. *GEOPHYSICS*, *61*(4), 971–986. https://doi.org/10.1190/1.1444046

Mccuaig, T. C., Beresford, S., & Hronsky, J. (2010). Translating the mineral systems approach into an effective exploration targeting system. *Ore Geology Reviews*, *38*(3), 128–138. https://doi.org/10.1016/j.oregeorev.2010.05.008

Milligan, P. R. (2013). *The Youanmi Magnetotelluric (MT) transects: Youanmi Seismic/MT Workshop*.

Mole, D. R., Fiorentini, M. L., Cassidy, K. F., Kirkland, C. L., Thebaud, N., McCuaig, T. C., … Miller, J. (2015). CruMole, D. R., Fiorentini, M. L., Cassidy, K. F., Kirkland, C. L., Thebaud, N., McCuaig, T. C., … Miller, J. (2015). Crustal evolution, intra-cratonic architecture and the metallogeny of an Archaean craton. Geological Society, London, Special Publication. *Geological Society, London, Special Publications*, *393*(1), 23–80. https://doi.org/10.1144/SP393.8

Myers, J. S. (1995). The generation and assembly of an Archaean supercontinent: evidence from the Yilgarn craton, Western Australia. *Geological Society, London, Special Publications*, *95*(1), 143–154. https://doi.org/10.1144/GSL.SP.1995.095.01.09

Ogawa, Y., & Uchida, T. (1996). A two-dimensional magnetotelluric inversion assuming Gaussian static shift. *Geophysical Journal International*, *126*(1), 69–76. https://doi.org/10.1111/j.1365-246X.1996.tb05267.x

Reading, A. M., Kennett, B. L. N., & Dentith, M. C. (2003). Seismic structure of the Yilgarn Craton, Western Australia. *Australian Journal of Earth Sciences*, *50*(3), 427–438. https://doi.org/10.1046/j.1440-0952.2003.01000.x

Reading, A. M., Kennett, B. L. N., & Goleby, B. (2007). New constraints on the seismic structure of West Australia: Evidence for terrane stabilization prior to the assembly of an ancient continent? *Geology*, *35*(4), 379–382. https://doi.org/10.1130/G23341A.1

Robertson, K., Meqbel, N., & Thiel, S. (2018). An investigation into modeling parameters with the ModEM3DMT inversion code. Abstract, 24th EM Induction Workshop, Helsingør, Denmark.

Rodi, W., & Mackie, R. L. (2001). Nonlinear conjugate gradients algorithm for 2-D magnetotelluric inversion. *GEOPHYSICS*, *66*(1), 174–187. https://doi.org/10.1190/1.1444893

Rudnick, R. L., & Fountain, D. M. (1995). Nature and composition of the continental crust: A lower crustal perspective. *Reviews of Geophysics*. https://doi.org/10.1029/95RG01302

Selway, K. (2014). On the Causes of Electrical Conductivity Anomalies in Tectonically Stable Lithosphere. *Surveys in Geophysics*, *35*(1), 219–257. https://doi.org/10.1007/s10712-013-9235-1

Simons, F. J., van der Hilst, R. D., Montagner, J. P., & Zielhuis, A. (2002). Multimode Rayleigh wave inversion for heterogeneity and azimuthal anisotropy of the Australian upper mantle. *Geophysical Journal International*, *151*(3), 738–754. https://doi.org/10.1046/j.1365-246X.2002.01787.x

Simpson, F., & Bahr, K. (2005). *Practical magnetotellurics*. *Practical Magnetotellurics*. https://doi.org/10.1017/CBO9780511614095

Siripunvaraporn, W., Egbert, G., Lenbury, Y., & Uyeshima, M. (2005). Three-dimensional magnetotelluric inversion: Data-space method. *Physics of the Earth and Planetary Interiors*, *150*(1–3 SPEC. ISS.), 3–14. https://doi.org/10.1016/j.pepi.2004.08.023

Spratt, J., Dentith, M., Evans, S., & Gessner, K. (2014). A magnetotelluric survey across the Albany – Fraser Orogen and adjacent Yilgarn Craton , southwestern Australia. *GSWA Record 2014/6*, (April 2012).

Thiel, S. (2008). *Modelling and inversion of magnetotelluric data for 2-D and 3-D lithospheric structure, with application to obducted and subducted terranes*. University of Adelaide.

Thybo, H., & Artemieva, I. M. (2013). Moho and magmatic underplating in continental lithosphere. *Tectonophysics*. https://doi.org/10.1016/j.tecto.2013.05.032

Vielreicher, N. M., Groves, D. I., & McNaughton, N. J. (2016). The giant Kalgoorlie Gold Field revisited. *Geoscience Frontiers*, *7*(3), 359–374. https://doi.org/10.1016/j.gsf.2015.07.006

Wang, Q., Schiøtte, L., & Campbell, I. H. (1996). Geochronological constraints on the age of komatiites and nickel mineralisation in the Lake Johnston greenstone belt, Yilgarn Craton, Western Australia. *Australian Journal of Earth Sciences*, *43*(4), 381–385. https://doi.org/10.1080/08120099608728261

Weaver, J. T., Agarwal, A. K., & Lilley, F. E. M. (2000). Characterization of the magnetotelluric tensor in terms of its invariants. *Geophysical Journal International*, *141*(2), 321–336. https://doi.org/10.1046/j.1365-246X.2000.00089.x

Whitaker, A. J. (2001). Components and structure of the Yilgarn Craton, as interpreted from aeromagnetic data. In: Cassidy, K.F., et, al. (Eds.), 4th International Archaean Symposium 2001, Extended Abstracts. AGSO, pp. 536–538, Geoscience Australia Record 2001/37.

Witt, W. K., & Vanderhor, F. (1998). Diversity within a unified model for Archaean gold mineralization in the Yilgarn Craton of Western Australia: an overview of the late-orogenic, structurally-controlled gold deposits. *Ore Geology Reviews*, *13*(1–5), 29–64. https://doi.org/10.1016/S0169-1368(97)00013-9

Wyche, S., Nelson, D. R., & Riganti, A. (2004). 4350-3130 Ma detrital zircons in the Southern Cross Granite-Greenstone Terrane, Western Australia: Implications for the early evolution of the Yilgarn Craton. *Australian Journal of Earth Sciences*, *51*(1), 31–45. https://doi.org/10.1046/j.1400-0952.2003.01042.x

# Supplementary Data

Apparent resistivity and phase curves for the initial data set and fits for Model A and Model F.

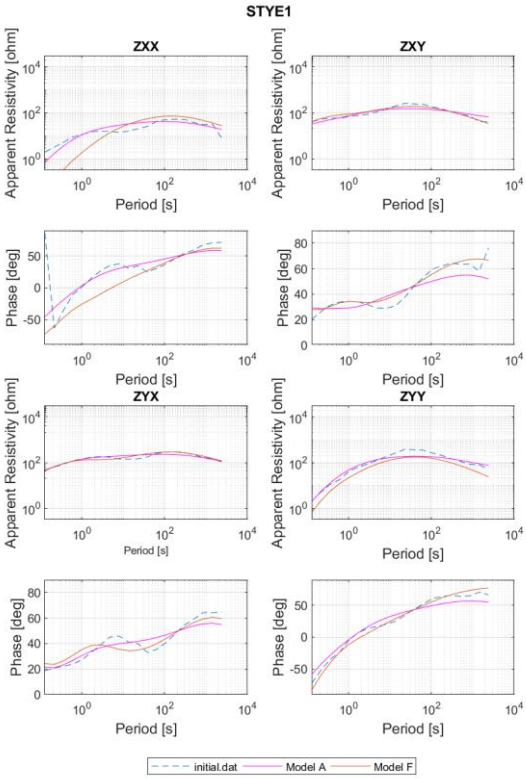


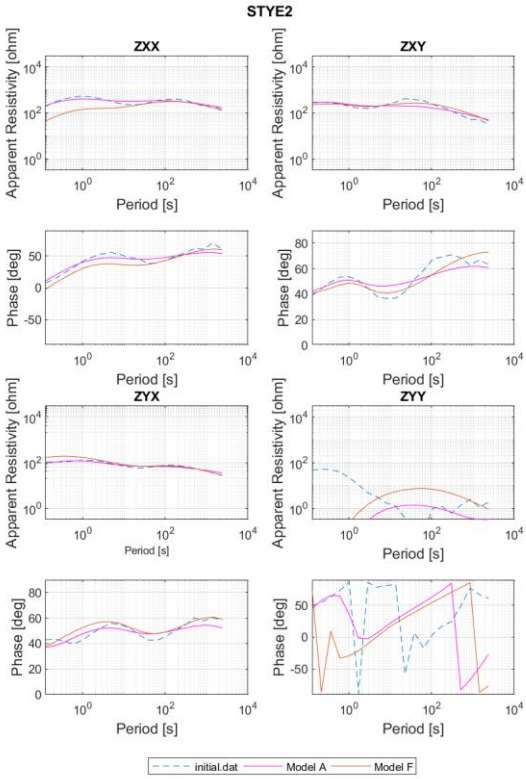


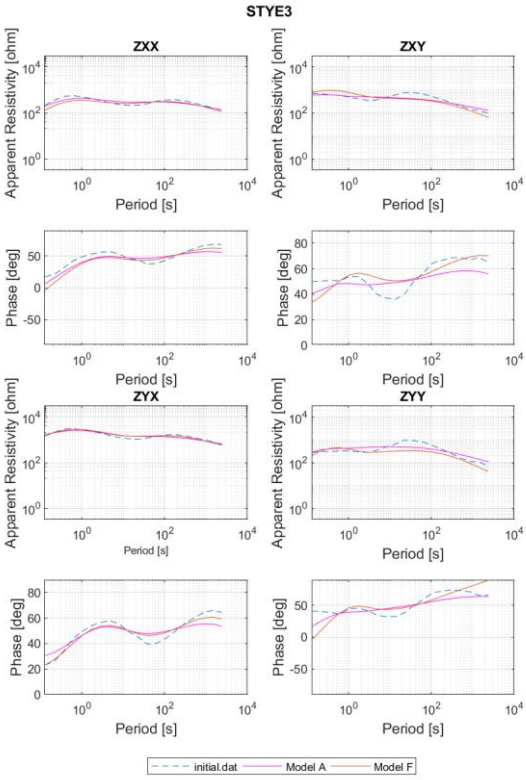


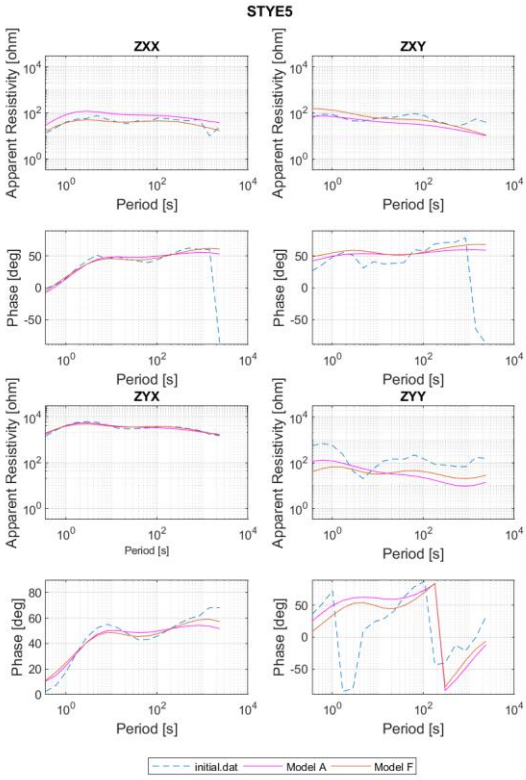

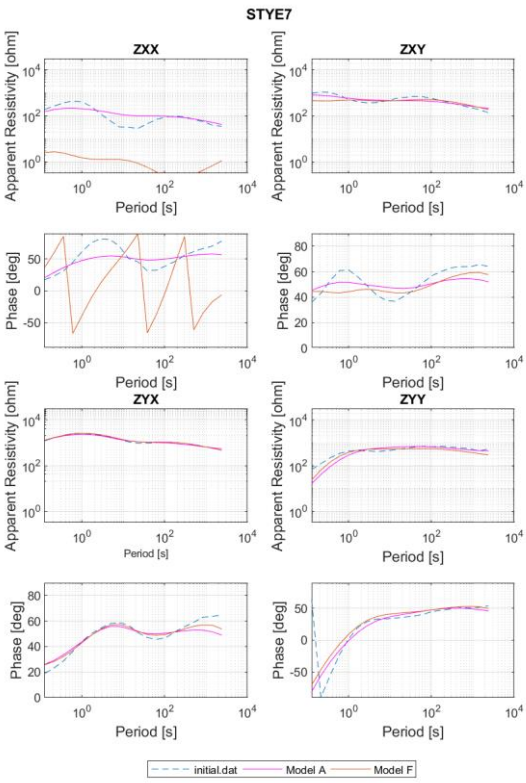
STYE7
ZXX
ZXY
ZYX
ZYY
Apparent Resistivity [ohm]
Phase [deg]
Period [s]
initial.dat
Model A
Model F

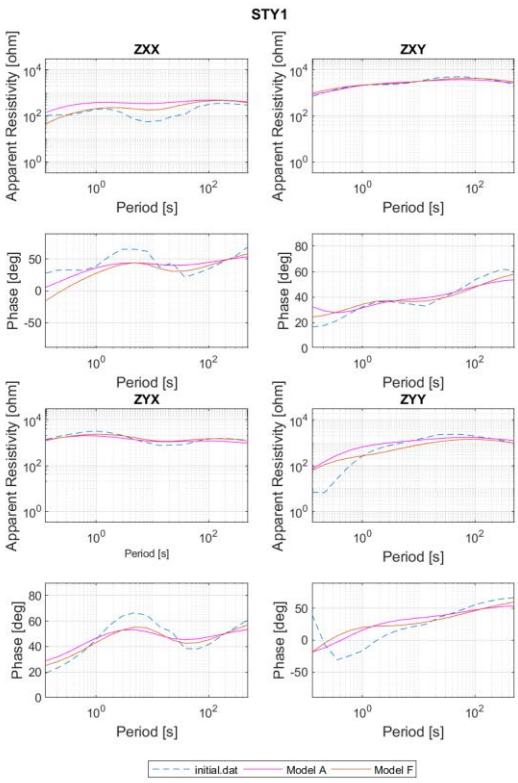
STY1
ZXX
ZXY
ZYX
ZYY
Apparent Resistivity [ohm]
Phase [deg]
Period [s]
initial.dat
Model A
Model F

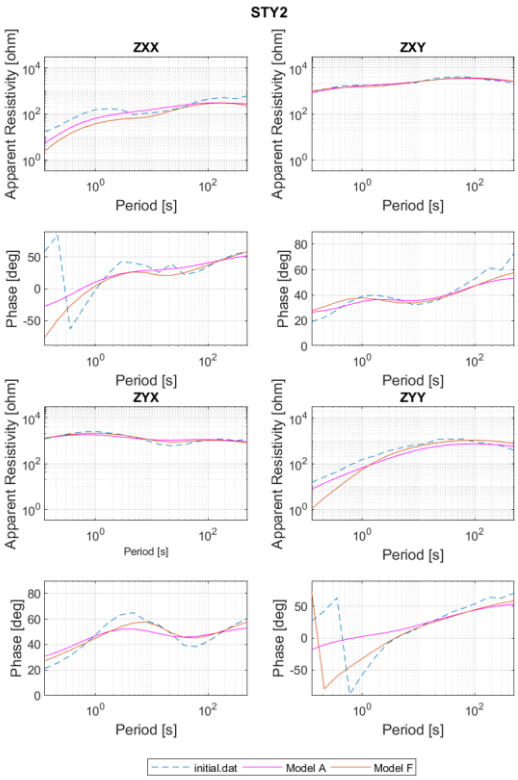
STY2
ZXX
ZXY
ZYX
ZYY
Apparent Resistivity [ohm]
Phase [deg]
Period [s]
initial.dat
Model A
Model F

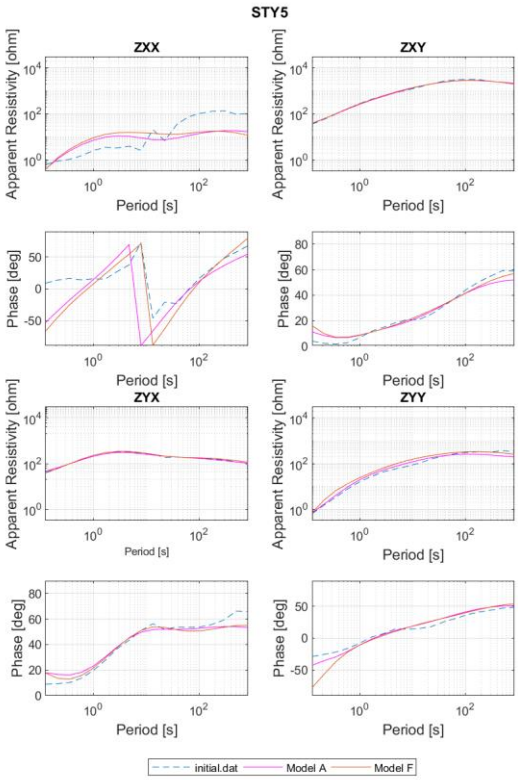
STY5
ZXX
ZXY
ZYX
ZYY
Apparent Resistivity [ohm]
Phase [deg]
Period [s]
initial.dat
Model A
Model F

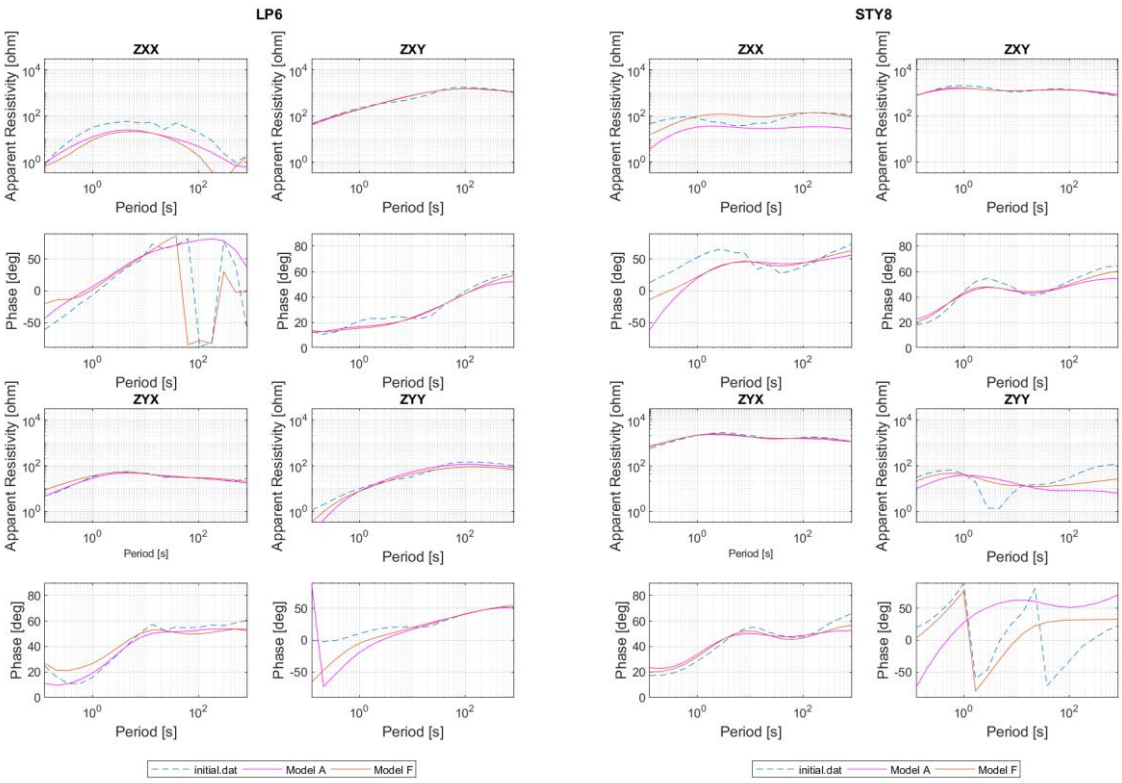
LP6
ZXX
ZXY
ZYX
ZYY
Apparent Resistivity [ohm]
Phase [deg]
Period [s]
initial.dat
Model A
Model F

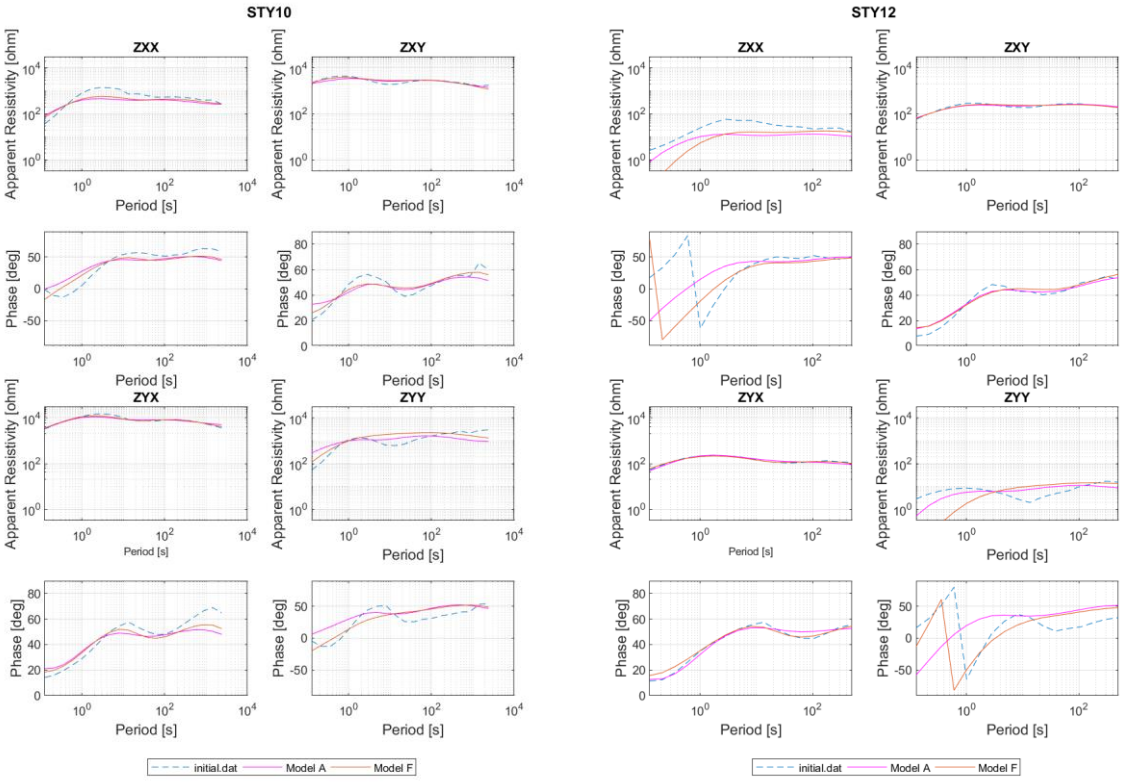
STY8
ZXX
ZXY
ZYX
ZYY
Apparent Resistivity [ohm]
Phase [deg]
Period [s]
initial.dat
Model A
Model F


STY10
ZXX
ZXY
ZYX
ZYY
Apparent Resistivity [ohm]
Phase [deg]
Period [s]
initial.dat
Model A
Model F


STY12
ZXX
ZXY
ZYX
ZYY
Apparent Resistivity [ohm]
Phase [deg]
Period [s]
initial.dat
Model A
Model F

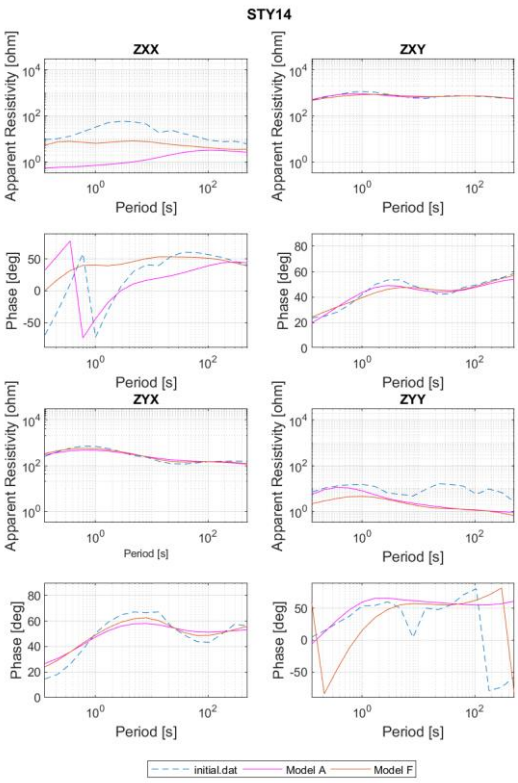
STY14
ZXX
ZXY
ZYX
ZYY
Apparent Resistivity [ohm]
Phase [deg]
Period [s]
initial.dat
Model A
Model F

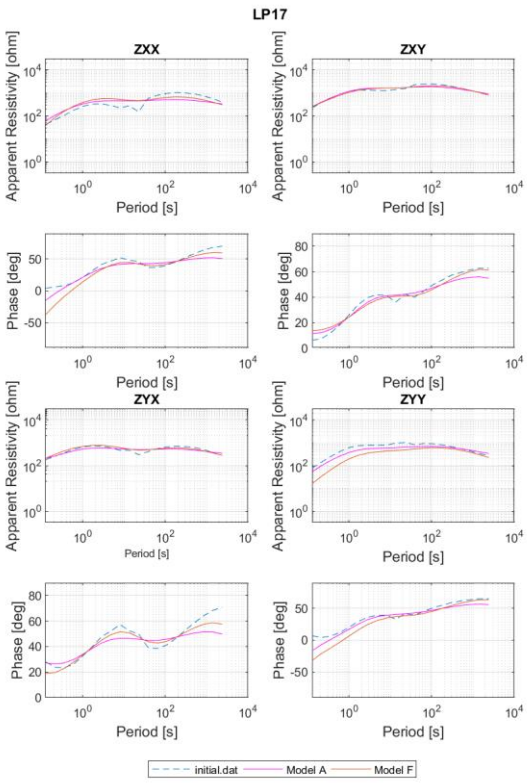
LP17
ZXX
ZXY
ZYX
ZYY
Apparent Resistivity [ohm]
Phase [deg]
Period [s]
initial.dat
Model A
Model F

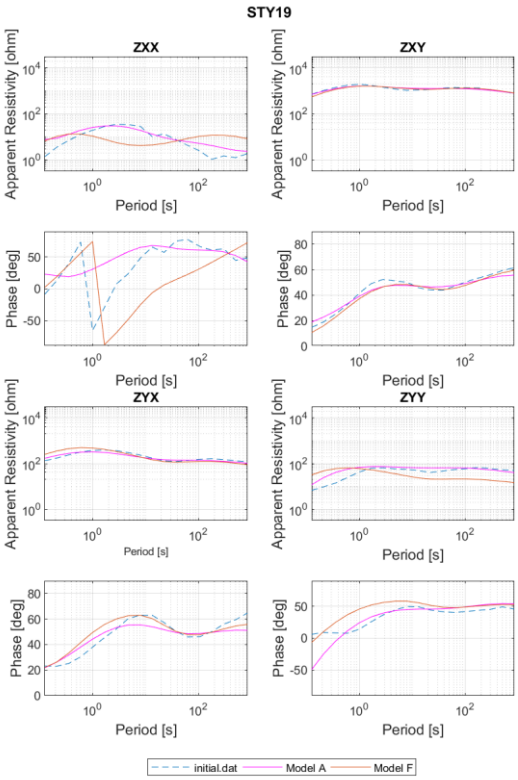
STY19
ZXX
ZXY
ZYX
ZYY
Apparent Resistivity [ohm]
Phase [deg]
Period [s]
initial.dat
Model A
Model F

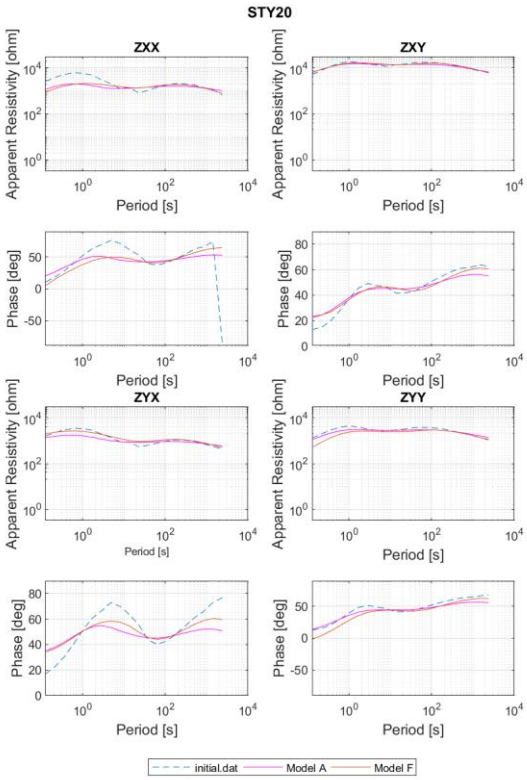
STY20
ZXX
ZXY
ZYX
ZYY
Apparent Resistivity [ohm]
Phase [deg]
Period [s]
initial.dat
Model A
Model F

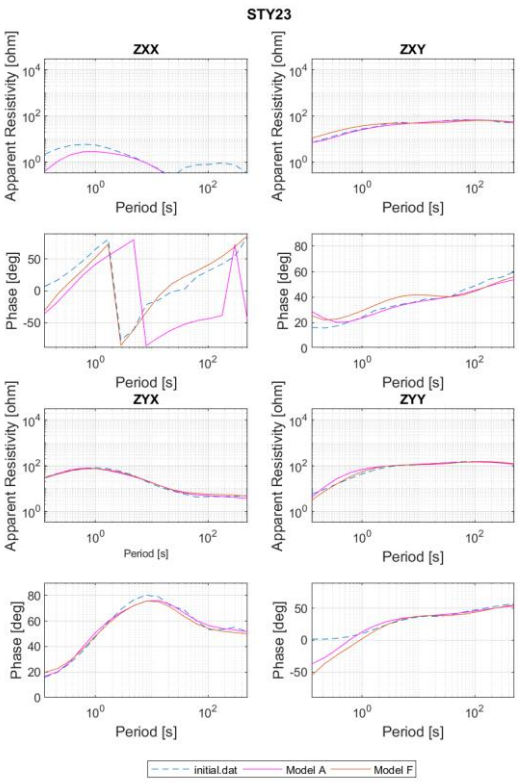
STY23
ZXX
ZXY
ZYX
ZYY
Apparent Resistivity [ohm]
Phase [deg]
Period [s]
initial.dat
Model A
Model F

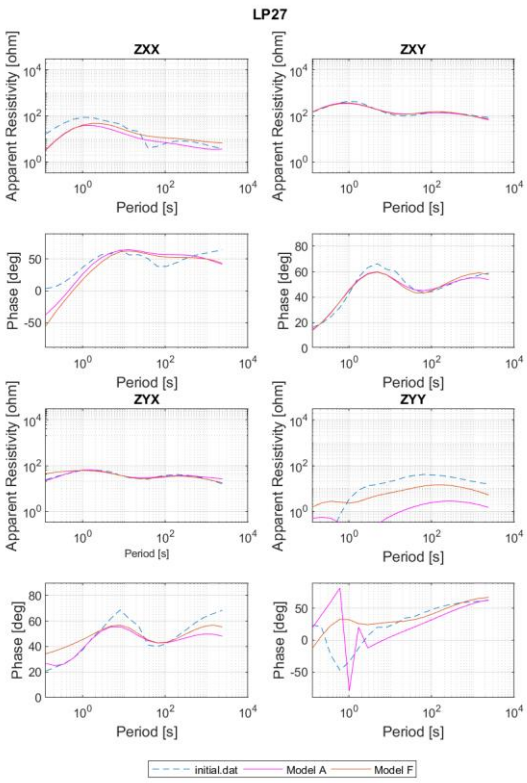
LP27
ZXX
ZXY
ZYX
ZYY
Apparent Resistivity [ohm]
Phase [deg]
Period [s]
initial.dat
Model A
Model F

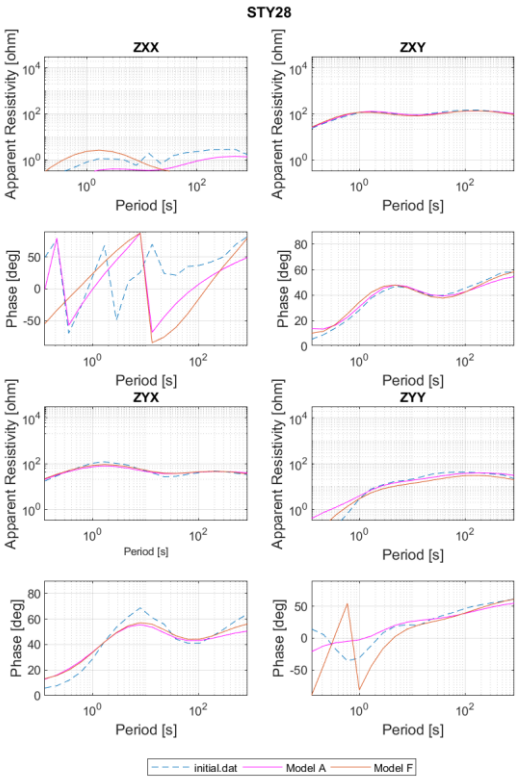
STY28
ZXX
ZXY
ZYX
ZYY
Apparent Resistivity [ohm]
Phase [deg]
Period [s]
initial.dat
Model A
Model F

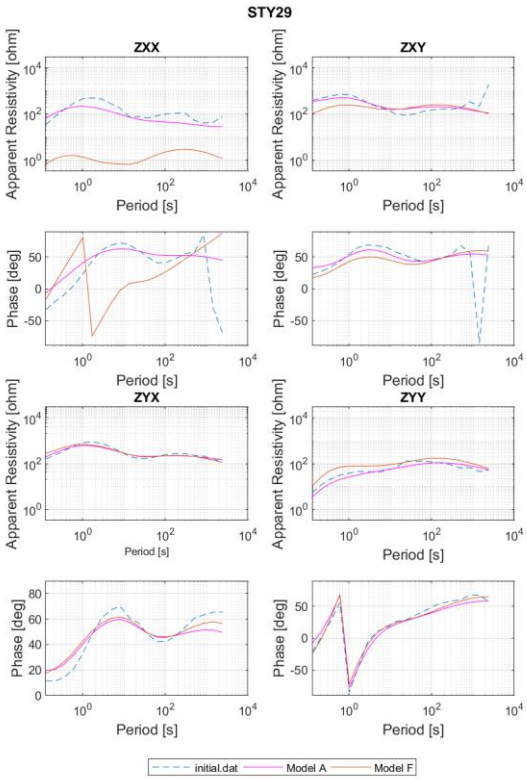
STY29
ZXX
ZXY
ZYX
ZYY
Apparent Resistivity [ohm]
Phase [deg]
Period [s]
initial.dat
Model A
Model F

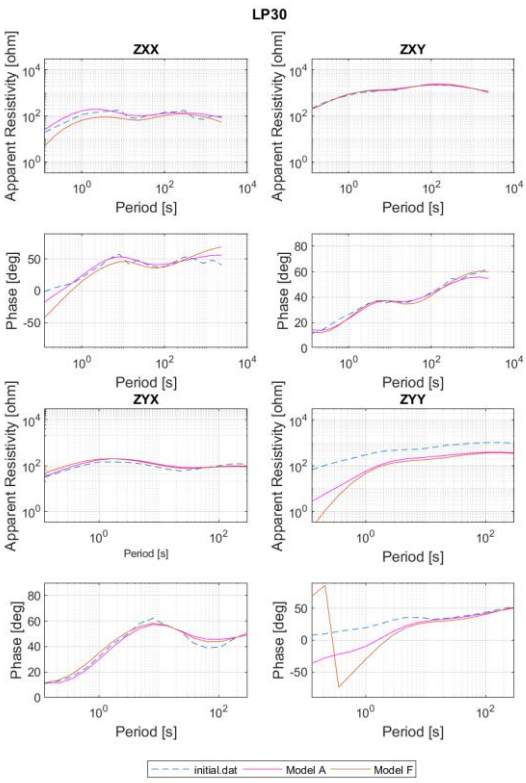
LP30
ZXX
ZXY
ZYX
ZYY
Apparent Resistivity [ohm]
Phase [deg]
Period [s]
initial.dat
Model A
Model F

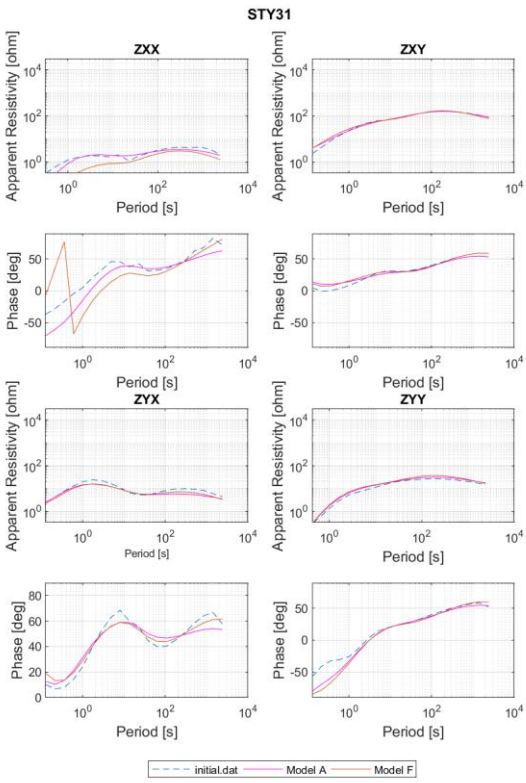
STY31
ZXX
ZXY
ZYX
ZYY
Apparent Resistivity [ohm]
Phase [deg]
Period [s]
initial.dat
Model A
Model F

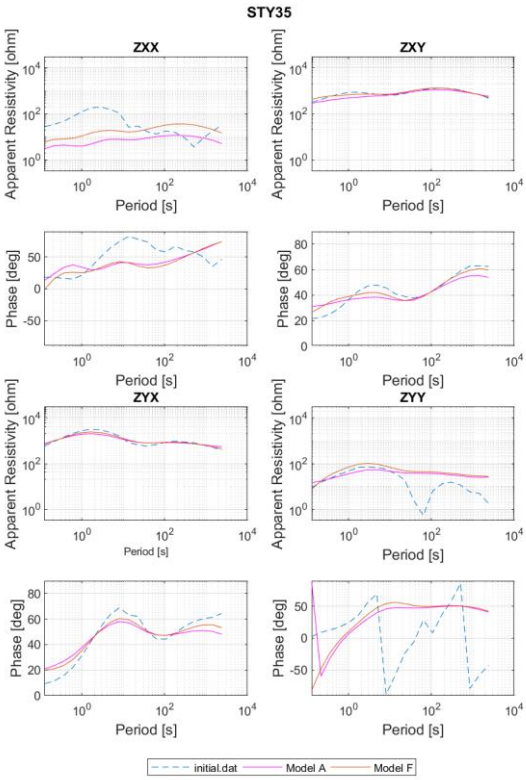
STY35
ZXX
ZXY
ZYX
ZYY
Apparent Resistivity [ohm]
Phase [deg]
Period [s]
initial.dat
Model A
Model F

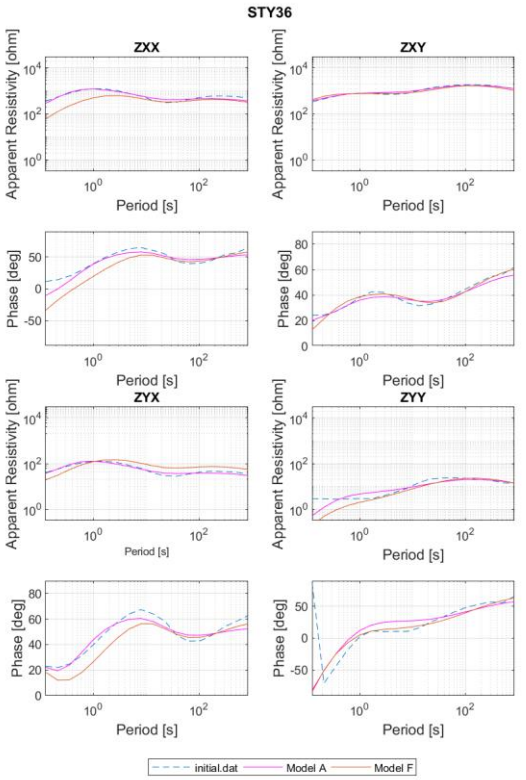
STY36
ZXX
ZXY
ZYX
ZYY
Apparent Resistivity [ohm]
Phase [deg]
Period [s]
initial.dat
Model A
Model F

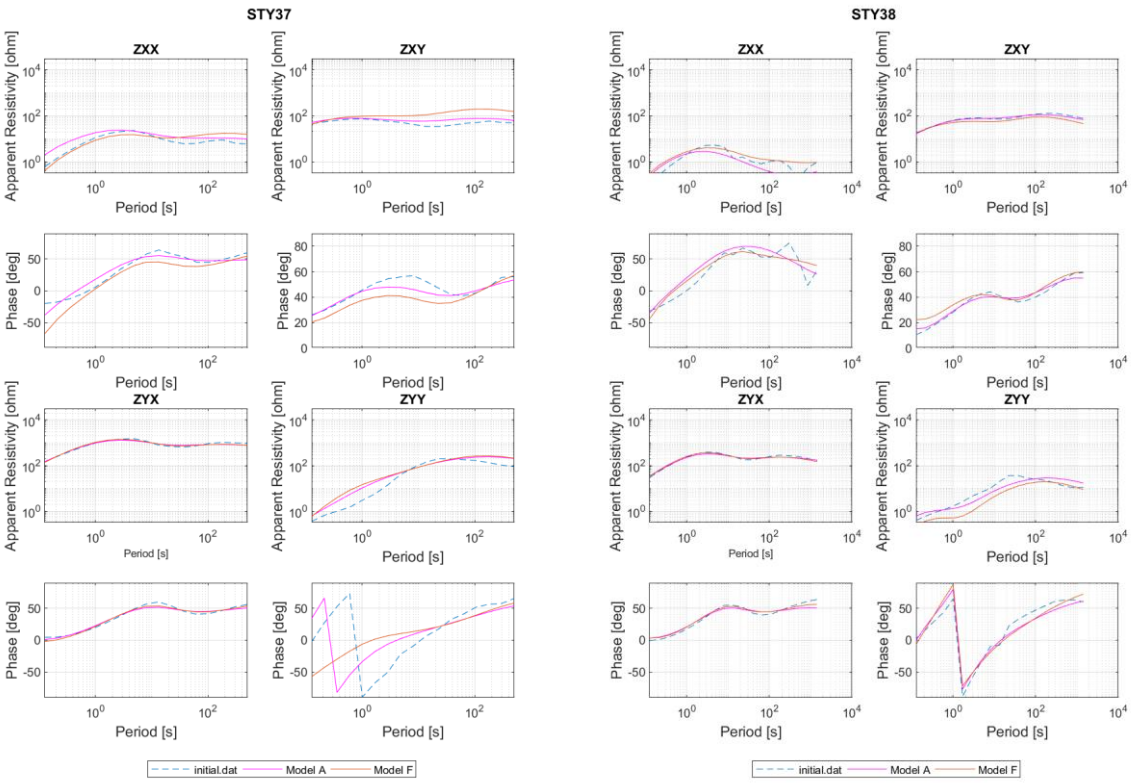
STY37
STY38
ZXX
ZXY
ZYX
ZYY
Apparent Resistivity [ohm]
Phase [deg]
Period [s]
initial.dat
Model A
Model F